JGR Space Physics

RESEARCH ARTICLE
10.1029/2025JA034045

Diagnosing the Rapid Loss of Outer Radiation Belt Electrons Due To Strong Chorus-Driven Wave-Particle Interactions Along an Electron Injection Path

S. Chakraborty[1], I. R. Mann[2], L. Olifer[2], R. Black[3,4], O. Allanson[3,5], I. J. Rae[1], L. G. Ozeke[2], and C. E. J. Watt[1]

[1]Department of Mathematics, Physics and Electrical Engineering, Northumbria University, Newcastle Upon Tyne, UK, [2]Department of Physics, University of Alberta, Edmonton, AB, Canada, [3]Department of Earth and Environmental Sciences, Environmental Mathematics, University of Exeter, Penryn, UK, [4]British Antarctic Survey (BAS), Cambridge, UK, [5]Space Environment and Radio Engineering (SERENE), Electronic, Electrical and Systems Engineering, School of Engineering, University of Birmingham, Birmingham, UK

Abstract Multi-spacecraft data demonstrate that intense chorus waves are excited during electron injection events that drive rapid radiation belt electron loss across a limited energy range from ∼100 to 300 keV on sub-drift timescales through strong pitch angle diffusion. We use a conjunction of Van Allen Probe A, B, and Arase spacecraft to study the variation of electron fluxes along an electron injection path in the energy range of ∼30 keV–1 MeV during the 20 April 2018, geomagnetic storm. At <∼100 keV, the 90° fluxes remained almost constant; for ∼100–300 keV, the fluxes decreased at all pitch angles; and at >∼300 keV, the fluxes showed a decrease following the injection closer to local midnight, and an increase further along the drift trajectory toward dawn. We calculate electron pitch angle and momentum diffusion coefficients in the observed waves using a quasi-linear approximation: fast losses only occurred at lower pitch angles at <∼100 keV but reached the core distribution for ∼100–300 keV. For >∼300 keV, the overall pitch angle diffusion is weak, but energy diffusion acts to increase the electron flux along the injection path. The results indicate that intense chorus waves drive loss on timescales of ∼10s of minutes through strong pitch angle diffusion that is localized in energy and local time, consistent with the observations. Overall, electron injection events should be associated with intense losses in a limited energy range, the resulting atmospheric impacts having strong local-time dependence, with preferential energy deposition in the morning sector during substorm injections.

Plain Language Summary Chorus waves are right-hand polarized electromagnetic waves that play a significant role in the Earth's electron radiation belt dynamics. These waves can both accelerate and scatter electrons and have been an important research topic for several decades. One effective approach to studying the role of these electromagnetic emissions on radiation belt dynamics is to use multi-spacecraft observations, as using in situ observations limits the measurements to a particular location at a particular time and thus cannot provide a more general overview of the systemic response. Toward that goal, here we use a conjunction of three spacecraft: Van Allen Probe A, Van Allen Probe B, and Arase to study the electron dynamics in the outer radiation belt during an electron injection event on 20 April 2018. To explain the observed flux variations, we further calculate the pitch angle and momentum diffusion coefficients using observed wave parameters. Our results show that intense chorus waves can drive rapid loss of radiation belt electrons through strong pitch angle diffusion on sub-drift timescales (∼10s of minutes) that is localized in both energy and local time. These results provide useful insights into the role of chorus-driven wave-particle interactions in the atmospheric loss of radiation belt electrons.

Key Points:

- Multi-spacecraft diagnose the evolution and energy-dependence of chorus wave-particle interactions along a dawnside injection path
- Fast ∼10-min timescale loss in a narrow energy band is observed, consistent with diffusion constrained by measured chorus wave parameters
- Energy-dependent competition between pitch angle and energy diffusion on sub-drift orbit timescales explains the observed flux variations

Supporting Information:

Supporting Information may be found in the online version of this article.

Correspondence to:

S. Chakraborty,
suman.chakraborty@northumbria.ac.uk

Citation:

Chakraborty, S., Mann, I. R., Olifer, L., Black, R., Allanson, O., Rae, I. J., et al. (2025). Diagnosing the rapid loss of outer radiation belt electrons due to strong chorus-driven wave-particle interactions along an electron injection path. *Journal of Geophysical Research: Space Physics*, *130*, e2025JA034045. https://doi.org/10.1029/2025JA034045

Received 4 APR 2025
Accepted 23 JUL 2025

Author Contributions:

Conceptualization: S. Chakraborty, I. R. Mann
Data curation: S. Chakraborty, R. Black
Formal analysis: S. Chakraborty, L. Olifer, R. Black
Investigation: S. Chakraborty, I. R. Mann, L. Olifer, R. Black, O. Allanson
Methodology: S. Chakraborty, I. R. Mann, L. Olifer, R. Black
Supervision: I. R. Mann
Validation: S. Chakraborty, I. R. Mann, L. Olifer, R. Black, O. Allanson
Visualization: S. Chakraborty, I. R. Mann, L. Olifer, R. Black, O. Allanson

1. Introduction

The Earth's Van Allen radiation belts are regions of trapped energetic charged particles that can experience rapid flux variation during geomagnetic storms, because of the complex balance between the effects of several competing wave-particle acceleration and loss processes (see e.g. the reviews by Ukhorskiy and Sitnov (2013); Ripoll et al. (2020); Kanekal and Miyoshi (2021); Y. Li et al. (2023)). In the outer radiation belt, energetic electrons are associated with risks to satellite electronics because of deep dielectric and surface charging (e.g., Baker et al., 2004; Ganushkina et al., 2021; Lai et al., 2018; Mateo-Velez et al., 2018; Minow et al., 2024). More recent studies have also proposed a potential connection between Van Allen belt electron precipitation and

Writing – original draft: S. Chakraborty, L. Olifer, R. Black, O. Allanson
Writing – review & editing: S. Chakraborty, I. R. Mann, L. Olifer, R. Black, O. Allanson, I. J. Rae, L. G. Ozeke, C. E. J. Watt

atmospheric and thermospheric dynamics (e.g., Capannolo et al., 2024; Duderstadt et al., 2021; Zhang et al., 2022) as well as a potential connection to the terrestrial climate, for example, catalytic destruction of ozone by HOx and NOx (e.g., Ozaki et al., 2024; Rodger et al., 2010; Thorne, 1977; Verronen et al., 2020). Understanding the radiation belt dynamics is therefore essential not only for mitigating space weather hazards but also for understanding the role of space radiation in the coupled climate system.

The complex dynamics of the Earth's radiation belts is maintained by a combination of different acceleration, transport, and loss mechanisms (Baker et al., 2004; M. K. Hudson et al., 2008; J. Li et al., 2019; Lejosne et al., 2022; Reeves et al., 2003; Ripoll et al., 2020; Summers et al., 2004). Two acceleration processes that are commonly examined in the radiation belts are local acceleration driven by cyclotron resonance with very low frequency (VLF) chorus waves (Allanson et al., 2021; Artemyev et al., 2016; Chakraborty et al., 2022; X. Gao, Chen, et al., 2022; X. Gao, Lu, et al., 2022; Horne & Thorne, 1998; Horne et al., 2005; Millan & Baker, 2012; Summers et al., 1998; Thorne et al., 2010; Ukhorskiy & Sitnov, 2013), and radial acceleration driven by drift resonance with ultra-low frequency (ULF) waves (Elkington et al., 1999; Elkington et al., 2003; Fälthammar, 1965; M. Hudson et al., 2000; Jaynes et al., 2018; Mann et al., 2013; Osmane et al., 2023, 2025; Ozeke et al., 2012; Ozeke et al., 2020; Ozeke, Mann, Murphy, et al., 2014; Ozeke, Mann, Turner, et al., 2014; Zhao et al., 2018). The radiation belt loss processes include either loss to interplanetary space through drift shell splitting and magnetopause shadowing (e.g., Tu et al., 2014; Turner et al., 2012), or atmospheric precipitation driven by wave-particle interactions with a variety of plasma waves, such as VLF chorus (e.g., Chakraborty et al., 2022; Drozdov et al., 2022; Shprits et al., 2016, etc.), hiss (e.g., Zhao et al., 2019), electromagnetic ion cyclotron (EMIC) waves (e.g., Ross et al., 2021), man-made VLF transmitter waves (e.g., Hua et al., 2020), and even ULF waves (e.g., Patel et al., 2025; Rae et al., 2018; Yin et al., 2023). In this paper, we focus on wave-particle interactions with VLF chorus waves, especially during periods where the electron flux is enhanced as a result of electron injections into the inner magnetosphere.

Energetic electron cyclotron resonance with chorus waves plays a significant role in shaping the outer radiation belt. Chorus waves are right-hand polarized electromagnetic waves having frequencies between the lower hybrid frequency and the local electron gyrofrequency (f_{ce}). These waves are typically separated into a lower band (0.1–0.5 f_{ce}) and an upper band (0.5–0.8 f_{ce}), with a wave power minimum being observed at ~0.5 f_{ce} (Koons & Roeder, 1990; J. Li et al., 2019; Tsurutani & Smith, 1974), although the presence of no-gap chorus waves and the lower or upper band only chorus waves have also been reported (e.g., Teng et al., 2019). Cyclotron resonance with the chorus waves breaks the first adiabatic invariant (magnetic moment) of the resonating electrons that leads to the change in their pitch angles and momentum. If the scattered pitch angles enter the loss cone, then the electrons are lost to the atmosphere within one-quarter of a bounce period. A quasi-linear approximation is often used to solve the Fokker-Planck equation and to estimate the pitch angle ($D_{\alpha\alpha}$), momentum (D_{pp}), and pitch angle-momentum ($D_{\alpha p}$) cross-diffusion coefficients with a diffusive formalism (e.g., Albert, 2005; Allanson et al., 2020, 2022; Allanson et al., 2024; Glauert & Horne, 2005; Horne et al., 2005; Lerche, 1968; Summers, 2005; Watt et al., 2022). However, such approximations are only valid when the wave power is low, and the wave spectrum is taken to be wide so that the resonant interaction can be considered to be a stochastic (diffusive) process (e.g., Albert, 2010; Allanson et al., 2024; Camporeale, 2015; Karpman, 1974).

During periods of enhanced geomagnetic activities, the chorus wave power can increase by several orders of magnitude above the ambient level (e.g., Breneman et al., 2011; Chakraborty et al., 2022; Cully et al., 2008; Hua, Bortnik, and Ma, 2023; Kellogg et al., 2011; Santolík et al., 2014; Tyler et al., 2019a, Tyler et al., 2019a; W. Li et al., 2011; Watt et al., 2019; Wilson III et al., 2011; Zhang et al., 2019; Zhang, Agapitov, et al., 2020; Zhang, Mourenas, et al., 2020), during which using quasi-linear theory cannot accurately predict the electron behavior. During such times, the wave-particle interactions can be in the nonlinear regime. Several previous studies have used non-linear theory to assess the impacts of such non-linear chorus wave-particle interactions on radiation belt dynamics during geomagnetic storms (e.g., Agapitov et al., 2015; Foster et al., 2017; Kondrashov et al., 2024; Kurita et al., 2018; Mozer et al., 2018; Shumko et al., 2018; Tsai et al., 2022; Zhang et al., 2019; Zhang et al., 2022). However, both the quasi-linear and non-linear approaches can be data-driven and use spacecraft observations as model inputs to provide electron flux or electron phase space density (PSD) as outputs (e.g., Albert et al., 2016; Claudepierre et al., 2020; Hua, Bortnik, Kellerman, et al., 2023; Saito et al., 2021). One of the major drawbacks of using in situ measurements for an event study is that it can only provide measurements at a

particular location at a particular time and thus cannot provide a more general overview of the systemic response. Nonetheless, multi-spacecraft observations can help to reveal a higher fidelity picture of the overall dynamics (for example, Colpitts et al., 2020; Miyoshi et al., 2022; Santolík et al., 2021).

Motivated by such an approach, in this work, we use a conjunction of three spacecraft to study outer radiation belt electron dynamics during a series of electron injection events. On 20 April 2018, an interplanetary shock hit the Earth's magnetosphere that led to a moderate geomagnetic storm. During the course of the storm, multiple substorms of moderate to strong intensity occurred which led to several electron injections into the inner magnetosphere. Between 0900 and 1230 UT, Van Allen Probe B, Van Allen Probe A, and Arase were close to the midnight, dawn, and pre-noon local time sectors within similar L-shell ranges. This created a powerful conjunction between the three spacecraft along the drift paths of newly injected electrons. We use particle and electromagnetic wave data from this conjunction to study the observed electron dynamics and use additional data and an assessment of the relevant diffusion coefficients to study the observations in the context of intense chorus wave-particle interactions during injection events. The results demonstrate that very fast, ∼10 min, timescale losses can occur to the atmosphere during such times.

2. Data and Instrumentation

In this work, we used electron flux and electromagnetic wave measurements from both of NASA's twin Van Allen Probes and JAXA's Arase spacecraft. For Van Allen Probes, we used 11 s resolution pitch angle resolved (Level 3) electron flux measurements from the Magnetic Electron Ion Spectrometer (MagEIS) instrument in the Energetic Particle, Composition and Thermal plasma (ECT) suite which measures electron fluxes at energies from 30 keV to 4 MeV (Baker et al., 2013; Blake et al., 2013; Spence et al., 2013). For the Arase spacecraft, we used the ∼1 min resolution pitch angle resolved (Level 3) electron flux measurements from the High-Energy Particle (HEP) instrument that measures electron fluxes at energies from 70 keV to 2 MeV (Higashio et al., 2018).

To study the plasma waves, we used the survey mode (∼6 s resolution) wave magnetic field power spectral density measurements from the Electric and Magnetic Field Instrument Suite and Integrated Science (EMFISIS) instrument, which records wave power over 65 logarithmically spaced frequency bins from 1 Hz to 12 kHz (C. A. Kletzing et al., 2013; C. Kletzing et al., 2023). In this study, we specifically examined the whistler-mode chorus waves, which were selected using the following criteria: (a) the spacecraft is outside the plasmasphere, identified by the background plasma density being less than 30/cm^3 (Ripoll et al., 2022), (b) the magnetic field wave power spectral density was greater than 10^{-9} nT^2/Hz (Bingham et al., 2018; Hartley et al., 2015, 2016, 2019, 2023; W. Li et al., 2014; Malaspina et al., 2020; Wang et al., 2019), and (c) the wave ellipticity and planarity were greater than 0.5 (Santolík et al., 2002, 2003). After identification of the chorus waves, the wave power was calculated by integrating the power spectral density between 0.1 and 0.8 f_{ce}, where f_{ce} is the equatorial electron gyrofrequency.

In addition to the survey mode data, we also used the high-resolution burst-mode data from the EMFISIS instrument to provide high-resolution wave magnetic field power spectral densities when available. The burst-mode data provides the full set of waveform measurements within the 5.968s duration packet. However, this high-resolution data is not available continuously due to the high data volume (C. Kletzing et al., 2023). Each 5.968s burst waveform record of Bu, Bv, and Bw, which consists of 208,896 samples each, was split up into 1,024-point segments (∼0.03s). Each 1,024-point time series was then multiplied by a Hanning window function. A Fast Fourier Transform (FFT) was then applied to project the signal into the frequency domain. Due to a slight misalignment between the true U, V, W planes and the instruments' axes, the FFT must be multiplied by frequency dependent calibration coefficients, provided in the Level 2 data (C. A. Kletzing et al., 2013). According to Parseval's theorem (Paschmann & Daly, 1998), to obtain the power spectral density, for all positive frequencies, the absolute value is taken and squared and then divided by the FFT frequency bandwidth. We also multiply by 2 to account for taking only positive frequencies. As the Hanning window introduces a weighting effect on the signal, particularly at the edges of the window, there will be power lost in the resulting spectra. Therefore, we also multiplied by a correction factor that accounts for this reduction in spectral power (Paschmann & Daly, 1998). The frequency was cut off at 12 kHz, to match the upper frequency limit used in the survey product. We have verified our processes on appropriate Van Allen Probe data to show that we can accurately reproduce the survey-mode results to high precision.

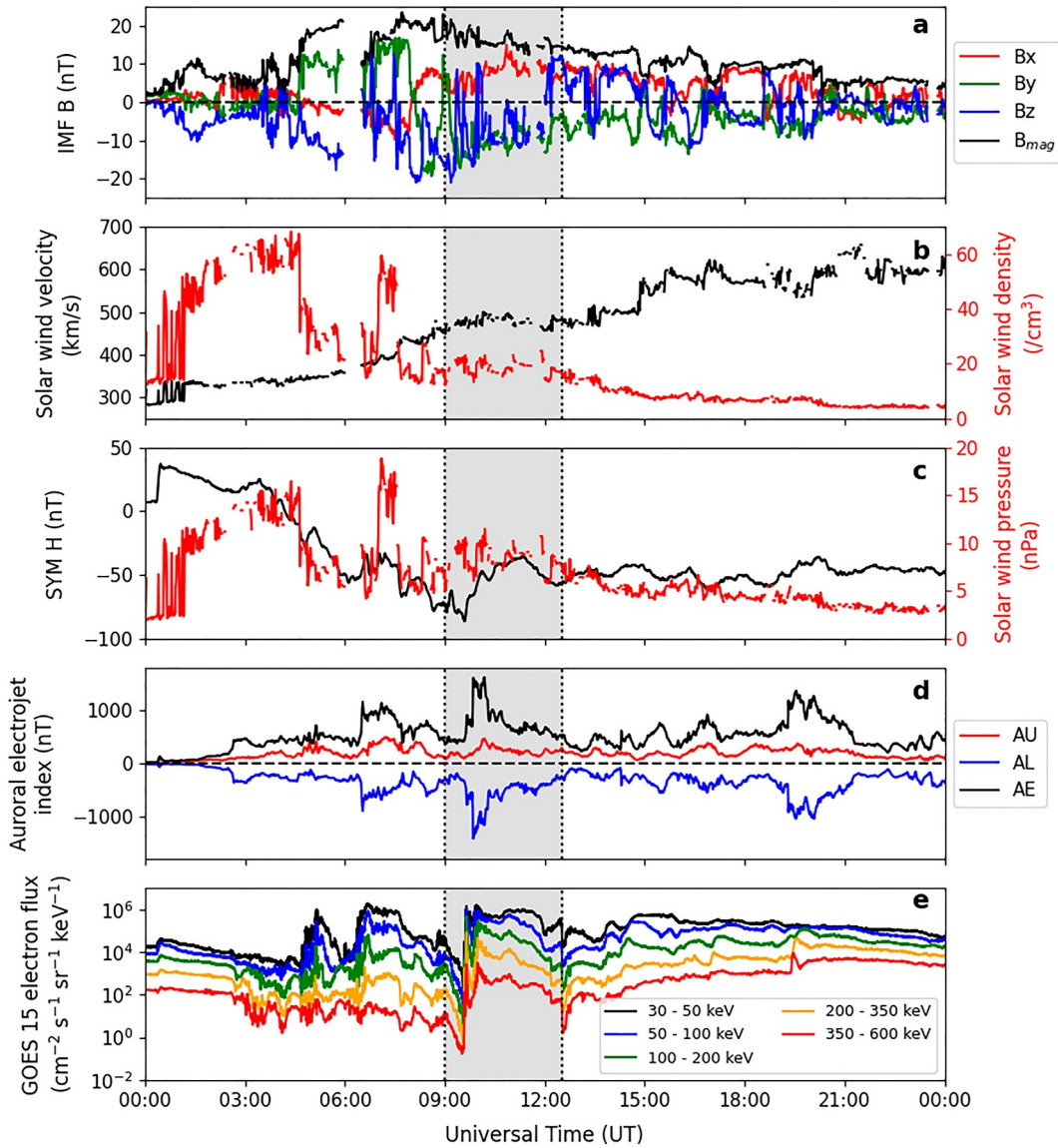

Figure 1. (a) x (red), y (green), and z (blue) component, and the magnitude (black) of the interplanetary magnetic field; (b) solar wind density (red) and solar wind velocity (black); (c) solar wind pressure (red) and SYM-H index (black); (d) AU (red), AL (blue) and AE (black) indices; and (e) GOES 15 electron flux in five energy channels (color coded) on 20 April 2018. In each panel, time in UT is along the *x*-axis and the parameters are plotted along the *y*-axis. The gray shaded region highlights the interval from 0900 to 1230 UT which is the focus of this study.

In this study, we also use 5-min resolution OMNI data (Papitashvili & King, 2020) to analyze variations in solar wind parameters and geomagnetic indices. Additionally, electron flux measurements from the GOES-15 spacecraft in geosynchronous orbit are utilized to examine electron flux variations during injection events.

3. Overview of the 20 April 2018 Geomagnetic Storm

On 20 April 2018, at ~0020 UT, an interplanetary shock hit the Earth's magnetosphere, which can be identified from the sudden increase in (a) solar wind density (Figure 1b), (b) solar wind dynamic pressure (Figure 1c), and (c) SYM-H index (Figure 1c). Following the shock impact, the z component of the interplanetary magnetic field remained mostly southward for a prolonged period, except for a very few brief northward turnings (Figure 1a). The solar wind driving led to a moderate geomagnetic storm, reaching a minimum SYM-H index of −88 nT at ~0930 UT (Figure 1c). During the course of the storm, multiple moderate to strong substorms occurred as

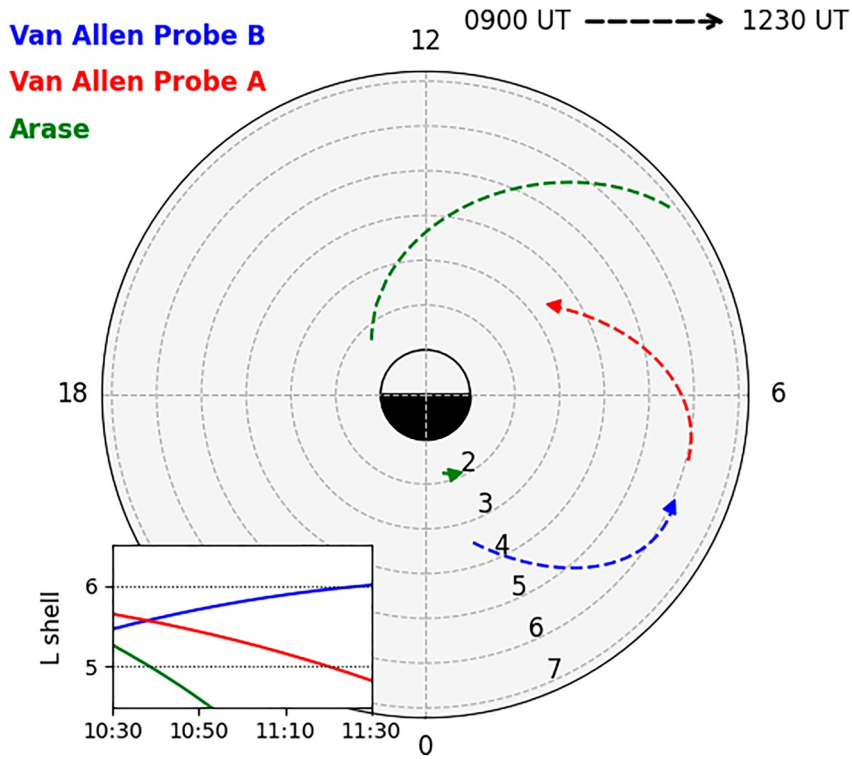

Figure 2. Dial plot showing the orbits of Van Allen Probe B (blue), Van Allen Probe A (red), and Arase (green) during the interval from 0900 to 1230 UT. For each orbit, the start time is 0900 UT and the end time is 1230 UT (shown by the black dashed arrow on the top right), and the Sun is at the top. The inset plot shows the L-shell coverage of the three spacecraft from 1030 to 1130 UT, during which the two Van Allen Probes were within similar L-shell ranges.

captured in the AL index, the strongest of which happened at ∼0951 UT with an AL index of −1,406 nT (Figure 1d). These substorms injected electrons into the inner magnetosphere as identified from GOES 15 electron flux measurements (Figure 1e).

In this study, we focus on the interval from 0900 to 1230 UT (highlighted by the gray-shaded region in Figure 1). During this interval, Van Allen Probe A and B were close to the midnight (1.19–4.41 MLT) and dawn (5.06–8.4 MLT) local time sectors, respectively, and the Arase spacecraft was further toward local noon (8.49–2.18 MLT, see Figure 2). Van Allen Probe B was outbound covering an L range of 3.47–6.06, Van Allen Probe A was inbound covering an L range of 6.05–3.39, and Arase was inbound covering an L range of 6.88–2.12, which included one perigee pass during this time interval. Here, L refers to the radial distance at which a magnetic field line crosses the equatorial plane, expressed in terms of Earth's radius (R_E). Further, during 1030–1130 UT, both the Van Allen Probes were within the L range of 5–6 (see the inset of Figure 2). The conjunction of these three spacecraft provided a powerful data set with which to study the evolution of the radiation belt electron dynamics along their drift trajectory within similar radial distances following the injection event and to assess the evolution of the injected electron fluxes in the context of the action of chorus-driven wave-particle interactions.

4. Electron Flux and Chorus Wave Observations

4.1. Electron Flux Dynamics

Figure 3 shows the temporal variation of the electron fluxes at 90° pitch angle as measured by (a) Van Allen Probe B, (b) Van Allen Probe A, and (c) Arase between 0900 and 1230 UT. Please note that the pitch angles used in this study are the local pitch angles. In each panel, time in UT is along the x-axis, electron differential flux is along the y-axis, and the color of each line represents the energy channel, as indicated on the right of each panel. The magnetic ephemeris information (L-shell, MLT, and MLAT) for each spacecraft is provided at the bottom of the

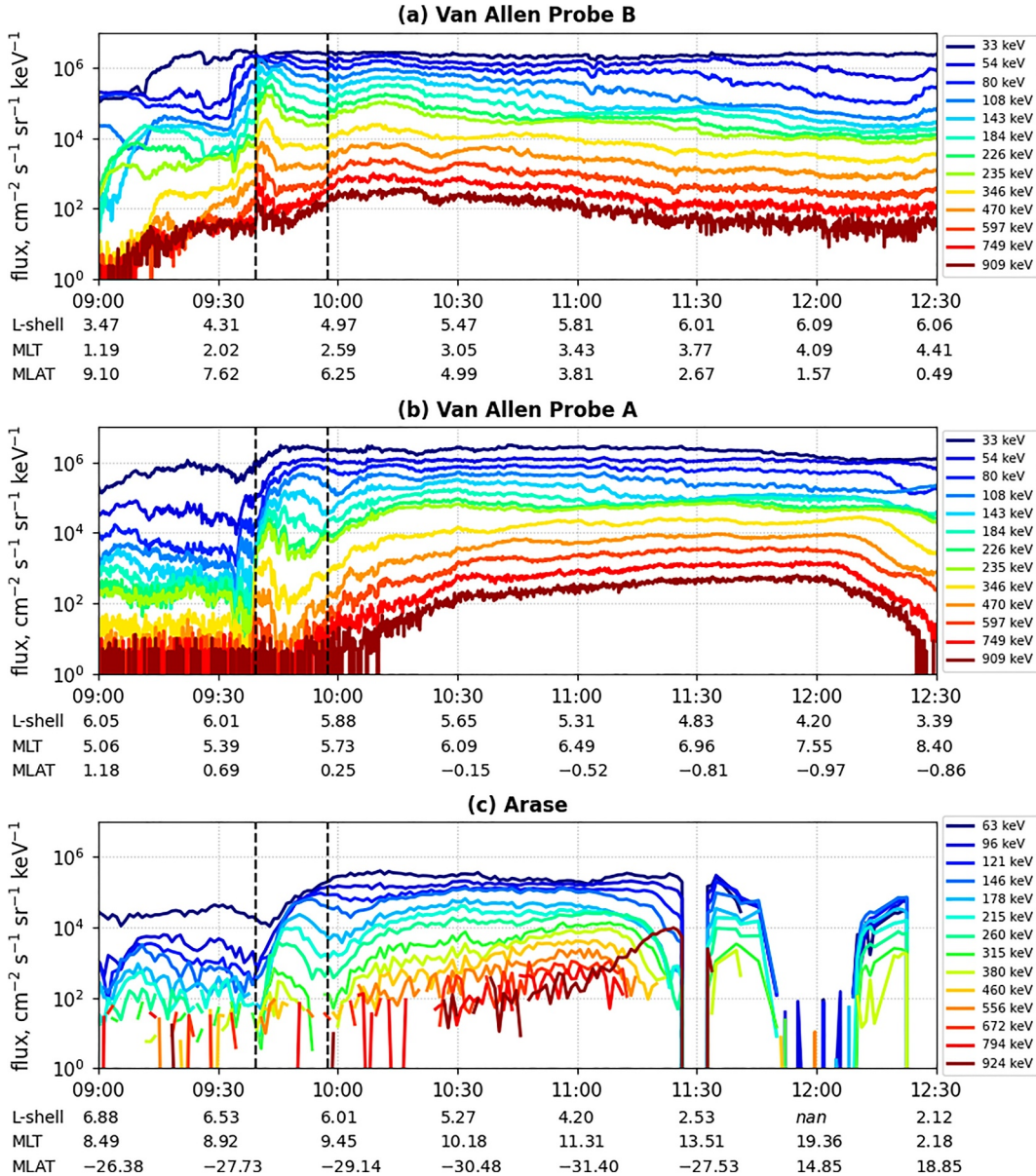

Figure 3. 90° electron flux measured by (a) Van Allen Probe B, (b) Van Allen Probe A, and (c) Arase from 0900 to 1230 UT at different energy channels (color coded). In each panel, time in UT is along the *x*-axis and differential electron flux on a logarithmic scale is along the *y*-axis. Magnetic ephemeris information (L-shell, MLT, and MLAT) of each spacecraft is provided along the *x*-axis of the corresponding panels. The dashed vertical lines in each panel indicate the time of electron injections associated with substorm events during this interval.

corresponding panels. The dashed vertical lines in each panel denote the time of electron injections associated with substorm events during this interval.

As shown in Figure 3a, Van Allen Probe B, which was close to the midnight local time sector observed two dispersionless injections, the first one at ∼0940 UT across a wide range of energies (∼30 keV–1 MeV), and the second one at ∼0951 UT of a smaller magnitude and spanning a comparatively narrower range of energies (∼30–500 keV). In comparison, Van Allen Probe A (Figure 3b) and Arase (Figure 3c), which were close to the dawn and pre-noon local time sectors, respectively, observed both the electron injections as energy-dispersed events, with electrons at higher energies exhibiting an enhancement in the flux ahead of electrons at lower energies. Please note that the electron flux at the locations of Van Allen Probe A (Figure 3a) and Van Allen Probe B (Figure 3b)

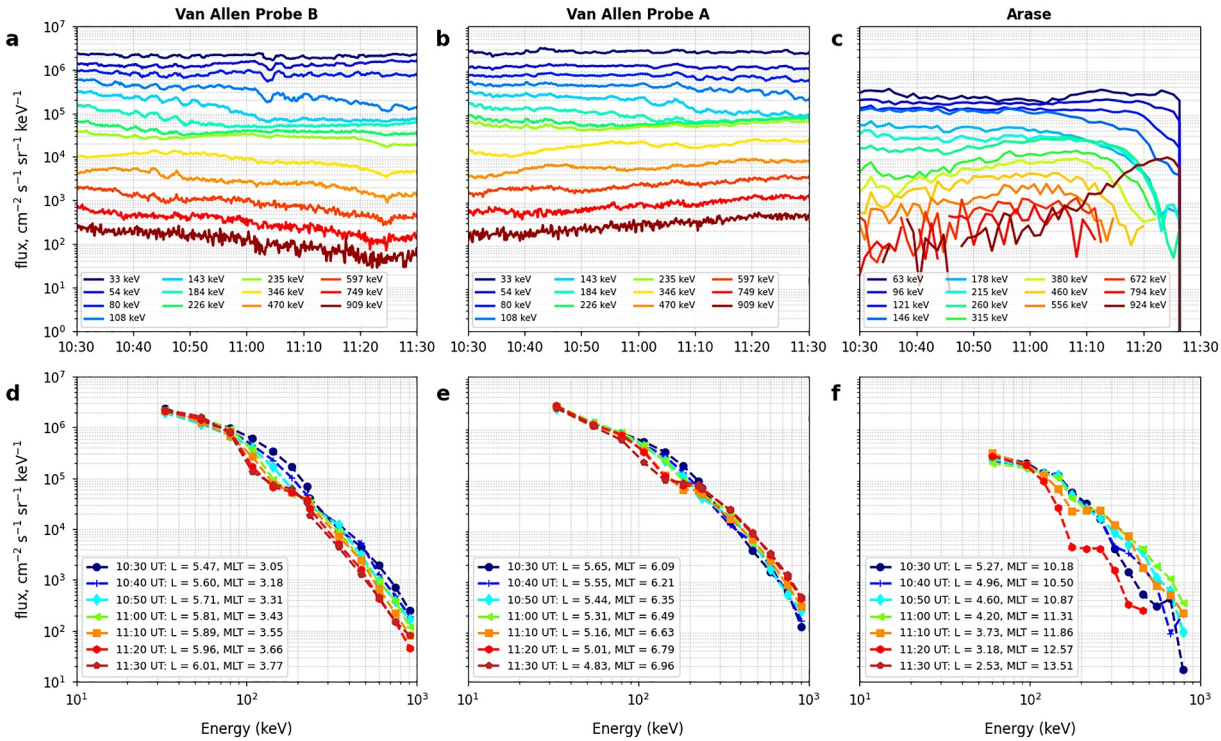

Figure 4. 90° electron flux measured by (a) Van Allen Probe B, (b) Van Allen Probe A, and (c) Arase from 1030 to 1130 UT at different energy channels (color coded) in a similar format to Figure 3. Energy spectra at seven specific sequential epochs from 1030 to 1130 UT, separated in time by 10 min (color coded), as measured by (d) Van Allen Probe B, (e) Van Allen Probe A, and (f) Arase. In each panel of the bottom row, electron energy in keV is along the *x*-axis and electron flux on a logarithmic scale is along the *y*-axis.

exhibit enhancements at energies less than ∼200 keV during ∼0930–0940 UT. However, during this interval, Figure 1 doesn't show any enhancement (depletion) in the AU (AL) index. Therefore, we rule out the possibility of substorms being the reason behind the flux enhancement during this interval. We argue that the flux enhancement during this interval might be a manifestation of spatial flux variations.

Following the second injection at ∼0951 UT, the 90° electron fluxes observed at both Van Allen Probe B (Figure 3a) and Van Allen Probe A (Figure 3b) remained almost constant at lower energies (<100 keV) for a prolonged period. At medium energies (100–300 keV), the fluxes initially increased followed by more gradual decreases. At higher energies (>300 keV), the fluxes showed a gradual decrease at Van Allen Probe B, while they increased at Van Allen Probe A. Figure 3 clearly shows the energy-dependent variation of electron fluxes along the trajectory of all three spacecraft during this 3.5-hr window. However, after ∼1100 UT, the Arase spacecraft moved close to lower L-shell ranges, during which the measured electron fluxes became intermittent and noisy (Figure 3c). This is why we focus primarily on the flux variations observed at Arase before ∼1100 UT and exclude Arase observations after ∼1100 UT for further analysis to avoid mixing spatial and temporal variations. Before ∼1100 UT, the flux of <100 keV electrons remained almost constant, while the fluxes of >100 keV electrons exhibited a gradual flux increase (Figure 3c).

Figure 4 shows a zoomed-in version of the temporal flux variations and energy spectrum from 1030 to 1130 UT, where the energy-dependent flux dynamics during the injection event are shown more clearly. The top row shows the 90° flux variations as measured by Van Allen Probe B (Figure 4a), Van Allen Probe A (Figure 4a), and Arase (Figure 4c) in a similar format to Figure 3. The bottom row shows the energy spectrum at seven specific sequential epochs from 1030 to 1130 UT, each separated in time by 10 min, as measured by Van Allen Probe B (Figure 4d), Van Allen Probe A (Figure 4e), and Arase (Figure 4f). For each panel in the second row, electron energy in keV is along the *x*-axis, and 90° pitch angle electron flux is along the *y*-axis. The colors of the energy spectra denote the times at which they are measured.

Figure 4d, in particular, shows that at Van Allen Probe B, the 90° flux at energies less than 80 keV remains almost constant during the 1-hr interval from 1030 to 1130 UT. Fluxes at energies 80–235 keV show significant and rapid decreases, whereas those at energies greater than 235 keV show a more gradual decrease. Figure 4e shows that at Van Allen Probe A, at later times, a similar trend of decreasing flux variations is seen in the 30–235 keV energy range, while for energies greater than 235 keV, the fluxes show a gradual increase with time. For Arase, as mentioned before, we focus on the shorter time interval from 1030 to 1100 UT, which shows a flux variation as a function of energy similar to that observed by Van Allen Probe A.

Note that during this time interval (1030–1130 UT), both Van Allen Probe B and Van Allen Probe A were located within the same L-shell range of ∼5–6 but separated in MLT (see inset of Figure 2), while Arase was in the pre-noon sector on its outbound trajectory. Therefore, in the discussions that follow, we will focus on the observations made by Van Allen Probe B and Van Allen Probe A, as they provide a unique conjunction to study the behavior of radiation belt electrons along their drift trajectories. Although Figures 3 and 4 clearly show the variation of electron fluxes at 90° pitch angle, details of the electron dynamics across the full pitch angle distributions can provide important additional information about the nature of the assumed chorus-driven wave-particle interactions. Figure 5 shows the pitch angle distributions of electrons measured by Van Allen Probe B and Van Allen Probe A at selected energy channels at 80, 143, and 470 keV, representing the three energy ranges that exhibit the three different types of variations in the 90° flux between 1030 and 1130 UT, as seen in Figure 4.

Figure 5 panels (a, c, e) and (h, j, l) show the electron flux variations as a function of pitch angle between 1030 and 1130 UT. In each of these panels, time in UT is along the *x*-axis, pitch angle in degrees is along the *y*-axis, and the colorbars at the right denote electron fluxes. Figure 5 panels (b, d, f) and (i, k, m) show the pitch angle distributions at the same seven epochs as in Figure 4. In each of these panels, pitch angle in degrees is along the *x*-axis, flux is along the *y*-axis, and the color of each line plot denote the time at which they were measured. Figure 5 panels (g, n) show the pitch angle anisotropy index, calculated using the methodology as described in Chakraborty et al. (2024). Note that an anisotropy index of ≥1.05 represents a pancake distribution, and larger values of the anisotropy index indicate even further enhanced perpendicular anisotropy.

Pitch angle distributions of electron fluxes at 80 keV measured by both Van Allen Probe B (Figures 5a and 5b) and Van Allen Probe A (Figures 5h and 5i) show that although the 90° fluxes remain approximately constant during the 1-hr interval from 1030 to 1130 UT, fluxes at lower pitch angles decrease more rapidly, thereby increasing the pitch angle anisotropy, as can be seen from the anisotropy index (Figures 5g and 5n: blue curves). At 143 keV, the pitch angle distributions measured by Van Allen Probe B (Figures 5c and 5d) broaden with time (i.e., become less 90°-peaked), thereby reducing the overall anisotropy (Figure 5g: green curve). For Van Allen Probe A (Figures 5j and 5k), the overall evolution of the pitch angle distributions of electron fluxes at 143 keV is quite similar to that seen at Van Allen Probe A, although initially there is a slight increase in the anisotropy followed by a more gradual decrease (Figure 5n: blue curve). At 470 keV, for Van Allen Probe B (Figures 5e and 5f), the flux at almost all pitch angles decreases significantly, with a coincident overall reduction in the pitch angle anisotropy (Figure 5g: red curve). For Van Allen Probe A, at 470 keV (Figures 5l and 5m), the fluxes at all pitch angles increase with time, and they become flatter, thereby reducing the pitch angle anisotropy (Figure 5n: red curve). This flux increase at 470 keV appears to be consistent with flux increases as a result of energy diffusion which may be occurring between large amplitude chorus waves and the drifting injected population. This is discussed in detail further below.

4.2. Observation of Whistler-Mode Chorus Waves

Figure 6 shows the wave magnetic field PSD (panels a and f), and the associated wave properties: wave planarity (panels b and d), wave ellipticity (panels c and h) and the wave normal angle (panels d and i), the integrated wave power (P_{ch}) including both the lower and the upper band chorus waves (0.1–0.8 f_{ce}, f_{ce} being the equatorial electron gyrofrequency, panels e and k), and the ratio of the wave amplitude and the background magnetic field (panels f and l) between 1030 and 1130 UT as measured by Van Allen Probe B (left column) and Van Allen Probe A (right column). Here, we exclude chorus wave observations from Arase as during this interval, although it was within the same L-shell range of 5–6 for the initial ∼10 min, it later moved to lower L-shell ranges (c.f. the inset of Figure 2). In addition, Arase was located at a different MLT sector, closer to noon (Figure 2). Thus, although including Arase observations could have provided off-equatorial information about the wave dynamics, provided its high inclination orbit, it couldn't have explained the flux variations observed at the locations of the two Van

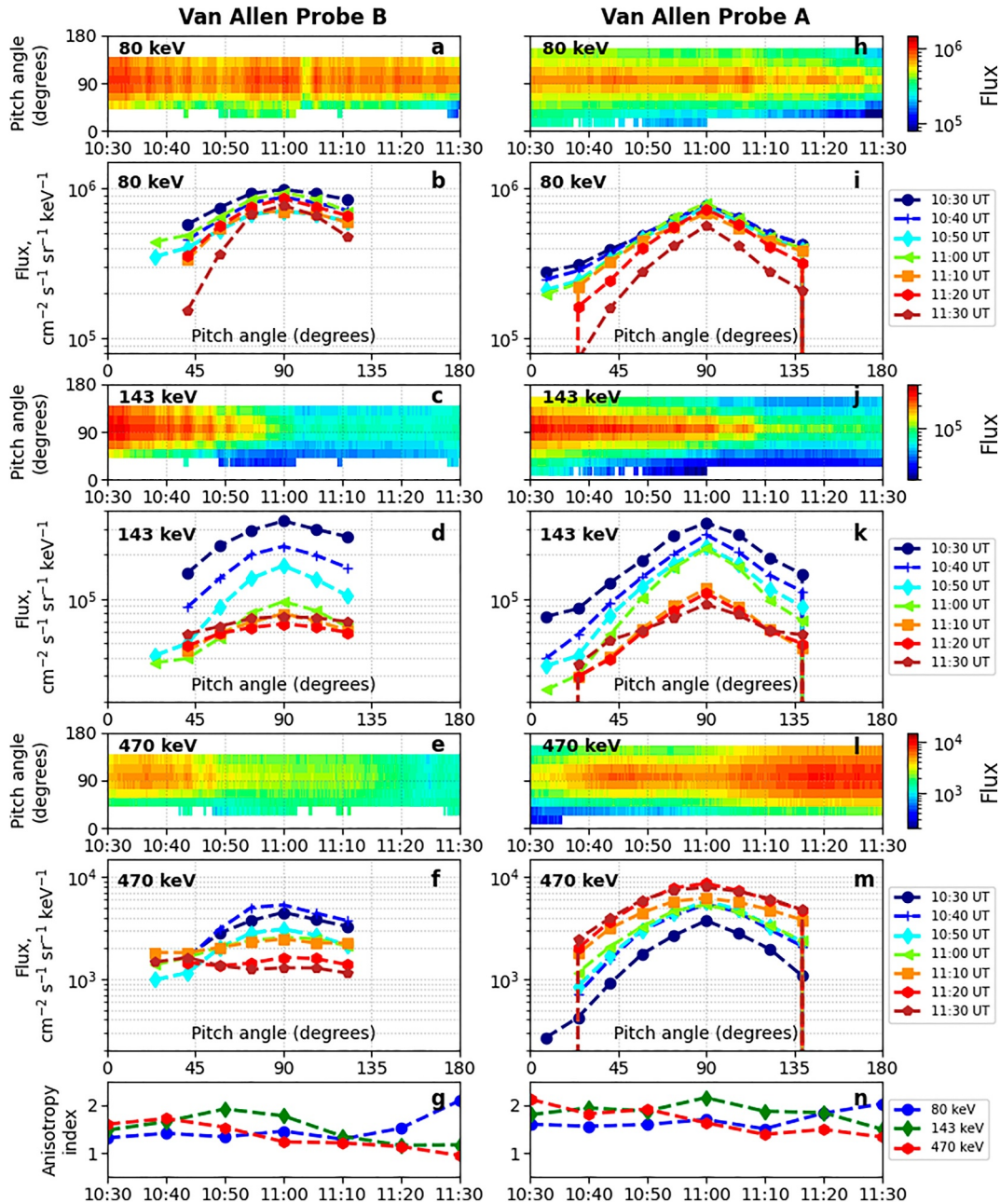

Figure 5. Pitch angle distribution of electron fluxes at (a, b, h, i) 80 keV, (c, d, j, k) 143 keV, and (e, f, l, m) 470 keV, measured by Van Allen Probe B (left column) and Van Allen Probe A (right column) from 1030 to 1130 UT. Panels (a, c, e, h, j, l) show the pitch angle distributions as a function of time (along the *x*-axis) and pitch angle (along the *y*-axis). The colorbars at the right of these panels denote the electron flux on a logarithmic scale. Panels (b, d, f, i, k, m) show the pitch angle distributions at the same seven epochs as in Figure 4. In these panels, pitch angle in degrees is along the *x*-axis and electron flux on a logarithmic scale is along the *y*-axis. Panels (g, n) show the pitch angle anisotropy index for 80 keV (blue), 143 keV (green), and 470 keV (red) electrons, calculated using the methodology as described in Chakraborty et al. (2024).

Allen Probes. In Figure 6 panels (a–d) and (g–j), time in UT is along the *x*-axis, frequency in Hz is along the *y*-axis, and the colorbars on the right represent the corresponding parameters. The dotted and dashed lines in each of these panels represent 0.1 and 0.8 f_{ce}, and 0.5 f_{ce}, respectively. In panels (e) and (k), time in UT is along the *x*-axis and the integrated wave power in nT^2 is along the *y*-axis. Similarly, in panels (f) and (l), time in UT is along the *x*-axis, and the ratio of the wave amplitude to the background magnetic field is along the *y*-axis.

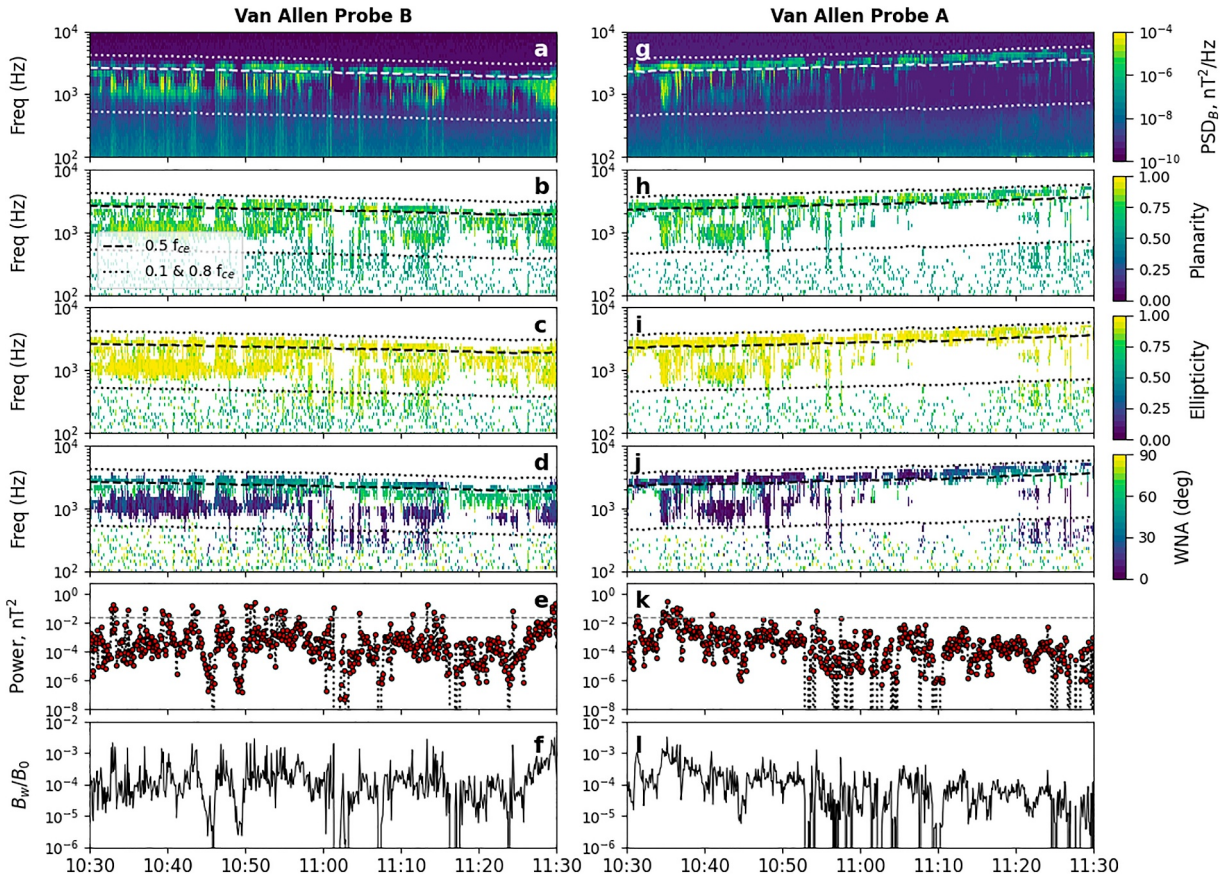

Figure 6. Magnetic field power spectral density (PSD) and the associated wave properties measured by Van Allen Probe B (left column) and Van Allen Probe A (right column) from 1030 to 1130 UT. Panels (a, g) show the wave magnetic field PSD in units of nT^2/Hz; (b, h) show wave planarity; (c, i) show wave ellipticity; and (d, j) show the wave normal angle in degrees. In these panels, time in UT is along the *x*-axis and frequency in Hz is along the *y*-axis. The colorbars at the right denote the corresponding parameters, and the dotted and dashed lines denote 0.1 and 0.8 f_{ce}, and 0.5 f_{ce}, respectively, where f_{ce} is the equatorial electron gyrofrequency. Panels (e, k) show the integrated wave power within the frequency range of 0.1–0.8 f_{ce}. The dashed horizontal black lines in these panels denote a wave power value of 2.25×10^{-2} nT^2, which indicates an approximate threshold for non-linear wave-particle interactions as prescribed by Zhang et al. (2018) and Mourenas et al. (2018). Panels (f, l) show the ratio of the wave amplitude to the background magnetic field.

Figure 6 panels (a) and (g) show strong wave activity within the frequency range of chorus waves, as can also be seen from the integrated wave power (Figures 6e and 6k). Chakraborty et al. (2022) statistically classified the whistler-mode chorus waves into two populations: an ambient population having $P_{ch} < 10^{-4}$ nT^2, and an intense population having $P_{ch} \geq 10^{-4}$ nT^2. From Figure 6e, we can see that the chorus waves were mostly intense ($P_{ch} \geq 10^{-4}$ nT^2) and sporadic along the trajectory of Van Allen Probe B, while at Van Allen Probe A (Figure 6k), the chorus waves were initially intense, but which later gradually decreased in power, although remaining close to 10^{-4} nT^2. Another interesting feature to note is that the chorus waves at both Van Allen Probe B and Van Allen Probe A are field aligned (low wave normal angles) at lower frequencies while becoming more oblique (larger wave normal angles) at higher frequencies (Figures 6d and 6j).

Figure 6 panels (a) and (e) also show that from 1030 to 1100 UT, the chorus wave power varied periodically along the trajectory of Van Allen Probe B, with a periodicity of ~4 min. Such periodic variations are also seen in the electron fluxes having energy <500 keV measured by Van Allen Probe B, the particle flux modulation demonstrating similar periodicity (Figure 4a). Such periodic variations are likely a consequence of local Pc5 mode ULF wave modulation of the electron fluxes, and correspondingly a modulation of the growth of the chorus waves (e.g., Shang et al., 2021; Watt et al., 2011), thereby exhibiting a cross-scale coupling between the large-scale ULF waves, local chorus wave growth, and the resulting wave-particle interactions (e.g., W. Li et al., 2011). Please note that such modulations of chorus wave power and electron fluxes are not observed by Van Allen Probe A, which was close to the dawn local time sector, although both the probes were within similar

L-shell ranges (c.f. inset of Figure 2). This suggests the cross-scale coupling to be a local phenomenon. However, further analysis of this feature is beyond the scope of the current paper, and we plan to investigate it in more detail in a follow-up paper.

5. Understanding the Effect of Wave-Particle Interactions on Injected Electron Dynamics

5.1. Calculation of Quasi-Linear Diffusion Coefficients

To assess the impact of the observed chorus waves (Figure 6) on the injected electron population, we compute the bounce-averaged pitch angle and momentum (energy) diffusion coefficients along with their cross terms ($D_{\alpha\alpha}$, D_{pp}, and $D_{\alpha p}$). The largest diffusion coefficients indicate regions where the influence of the waves on particle dynamics is expected to be the most significant. Consequently, this method is particularly well-suited for estimating the domains of influence, in terms of energy (E), and pitch angle (α), where chorus waves can most strongly affect the particle distributions. In this study, we use a computationally efficient approach for calculating the diffusion coefficients using a precomputed lookup table, as described in Hua et al. (2022). This method relies on tabulated values parameterized by key plasma and wave properties, including chorus wave power, as a function of frequency, the ratio of local electron plasma frequency to cyclotron frequency (fpe/fce), wave normal angle, and spatial location. By referencing this table, diffusion coefficients can be calculated in under one second, enabling rapid and accurate analysis. Studies demonstrate that important differences arise from calculating diffusion coefficients using event-specific (e.g., Ripoll et al., 2017) or observation-specific (e.g., Watt et al., 2019) combinations of wave and plasma parameters compared to the use of averaged wave or plasma models. We here adopt the approach of calculating diffusion coefficients at each 6s interval according to the observed plasma and wave characteristics. For this study, we use the measured magnetic field PSD between 100 Hz and 11.2 kHz, the measured background magnetic field, and the cold plasma density provided in the EMFISIS data files. We also assumed that the chorus waves are quasi-field-aligned, with the wave normal angle range between 0 and 15°. The results of these calculations are presented in Figures 7 and 8. Note that for the particular interval shown, the observed wave power was enhanced in both upper and lower bands, and thus both were used in the calculation.

5.2. Results and Discussion

Figure 7a shows a 5-min interval of the 6-s resolution of survey mode wave magnetic field PSD measured by Van Allen Probe B from 10:31 to 10:36 UT. Time in UT is along the x-axis and frequency in Hz is along the y-axis. The colorbar at the right shows the wave magnetic field PSD. Figure 7a shows periods of strong wave activity with PSD values as high as $\sim 10^{-2}$ nT^2/Hz, mostly in the lower band of chorus wave emissions below 0.5 f_{ce}. We choose the 6-s interval from 10:32:58 UT to 10:33:04 UT to show the high-resolution burst mode wave magnetic field PSD in Figure 7b, plotted in the same manner as in Figure 7a. Figure 7b shows several "rising tone" features in the lower band. We calculated the pitch angle ($D_{\alpha\alpha}$) and momentum (D_{pp}) diffusion coefficients during the same 6 s time interval, which we show in Figures 7c and 7e, respectively. In both panels, pitch angle in degrees is along the x-axis, electron energy in keV is along the y-axis, and the colorbars at the right denote the corresponding diffusion coefficients in s^{-1}. Figures 7c and 7d show clearly that both pitch angle and energy diffusion are stronger at lower pitch angles for electrons having lower energies and at larger pitch angles for electrons having higher energies, however, the overall energy diffusion being less than the pitch angle diffusion by more than an order of magnitude. This feature becomes more evident when the diffusion coefficients are plotted as a function of pitch angle at specific energies in Figures 7d and 7f. In Figures 7d and 7f, pitch angle in degrees is along the x-axis, the pitch angle and momentum diffusion coefficients in s^{-1} are along the y-axis, and each line plot corresponds to a specific electron energy denoted by different colors. Figure 7d shows clearly that for electrons having energies $<\sim$100 keV, the pitch angle diffusion coefficient is high (10^{-3} s^{-1}) for pitch angles $<\sim 50°$. At higher pitch angles, the diffusion coefficients drop by several orders of magnitude. For electrons in the energy range of $\sim$100–300 keV, the pitch angle diffusion coefficient is high ($\sim 10^{-3}$ s^{-1}) within the pitch angle range of $\sim 50°$–70°. For pitch angles $<\sim 50°$, the pitch angle diffusion coefficient is less by an order of magnitude, while for pitch angles $>70°$, the pitch angle diffusion coefficient falls rapidly by several orders of magnitude. For electrons having energies $>\sim$300 keV, the pitch angle diffusion coefficients are low suggesting weak pitch angle diffusion at these energies. Figure 7f shows that for electrons having energies $<\sim$100 keV, the momentum diffusion

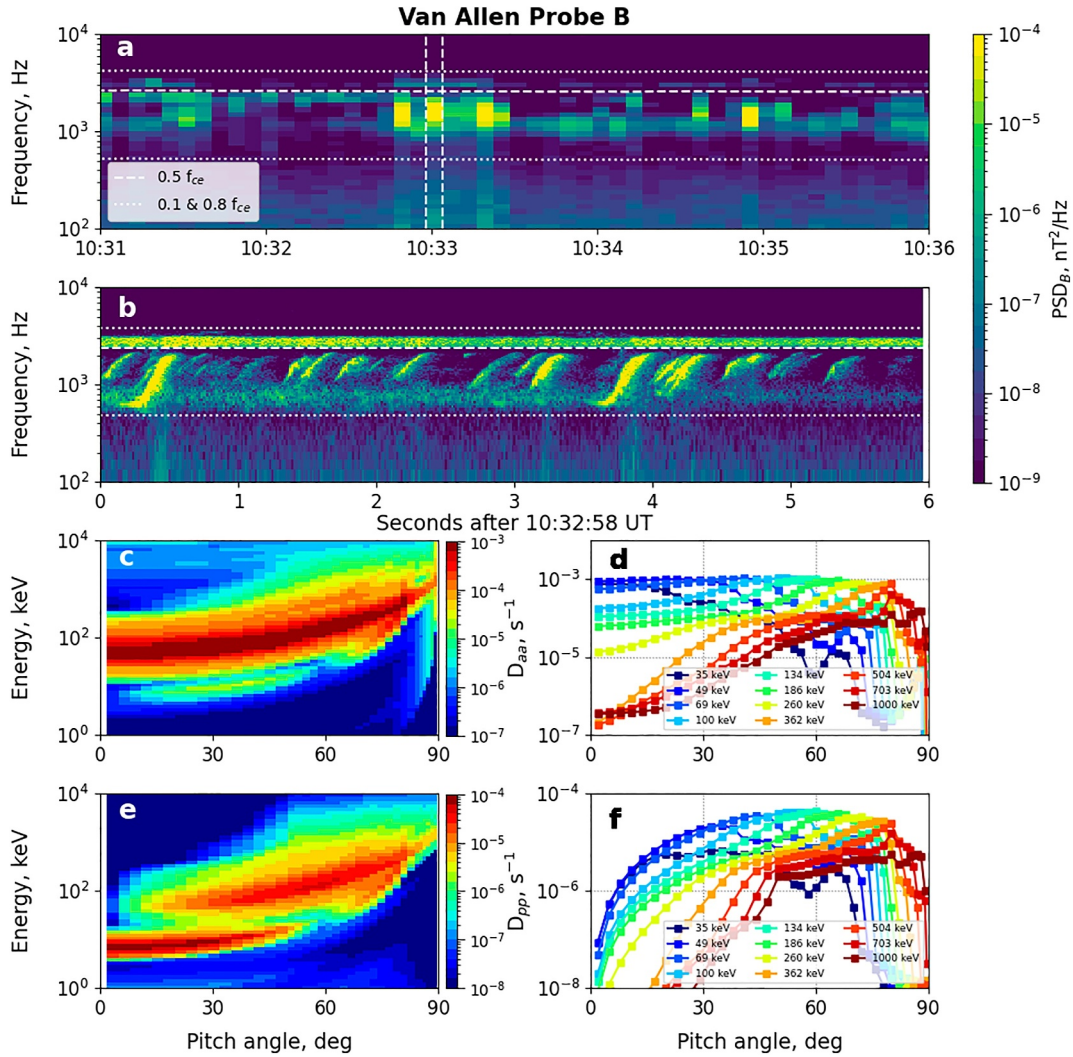

Figure 7. (a) Wave magnetic field power spectral density (PSD) during a 5-min interval from 1031 to 1036 UT; (b) 6-s high-resolution burst mode magnetic field PSD from 10:32:58 to 10:33:04 UT, the time interval marked by the vertical dashed lines in panel (a); pitch angle ($D_{\alpha\alpha}$) and momentum (D_{pp}) diffusion coefficients as a function of (c, e) pitch angle (along the *x*-axis) and energy (along the *y*-axis), and (d, f) pitch angle at specific electron energies (color coded) for Van Allen Probe B. The diffusion coefficients shown in panels (c–f) are calculated for the observed wave power frequency profile between the two vertical dashed lines in panel (a), as well as the background magnetic field strength of 196.886 nT and the cold plasma density of 3.561 cm^{-3}. The colorbars at the right of panels (a, b) denote the wave magnetic field PSD in nT^2/Hz, and the dotted and dashed horizontal lines denote 0.1 and 0.8 f_{ce}, and 0.5 f_{ce}, respectively. The colorbars at the right of panels (c, e) denote the corresponding diffusion coefficients in s^{-1}.

coefficient increases with pitch angle up to ∼45°, beyond which it reduces significantly. For electron having energies in the range of ∼100–300 keV, the momentum diffusion coefficient increases with pitch angle, being maximum at ∼60°–70°. For electrons with energies >∼300 keV, the momentum diffusion coefficient is significantly lower at lower pitch angles and higher at larger pitch angles.

In a similar fashion, Figure 8 (same format as Figure 7) shows a 6-min interval of the 6-s resolution survey mode wave magnetic field PSD from 10:33 UT to 10:39 UT (Figure 8a), burst mode magnetic field PSD for the 6-s interval from 10:35:12 UT to 10:35:18 UT (Figure 8b), pitch angle and momentum diffusion coefficients calculated during the same 6-s interval as a function of pitch angle and energy (Figures 8c and 8e), and the pitch angle and momentum diffusion coefficients for specific electron energies (Figures 8d and 8f), for Van Allen Probe A. Figure 8 shows a period of similar strong chorus wave activity in both the upper and lower bands. Again, the burst mode data shows repeated "rising tone" features in the lower band, but a more continuous emission in the

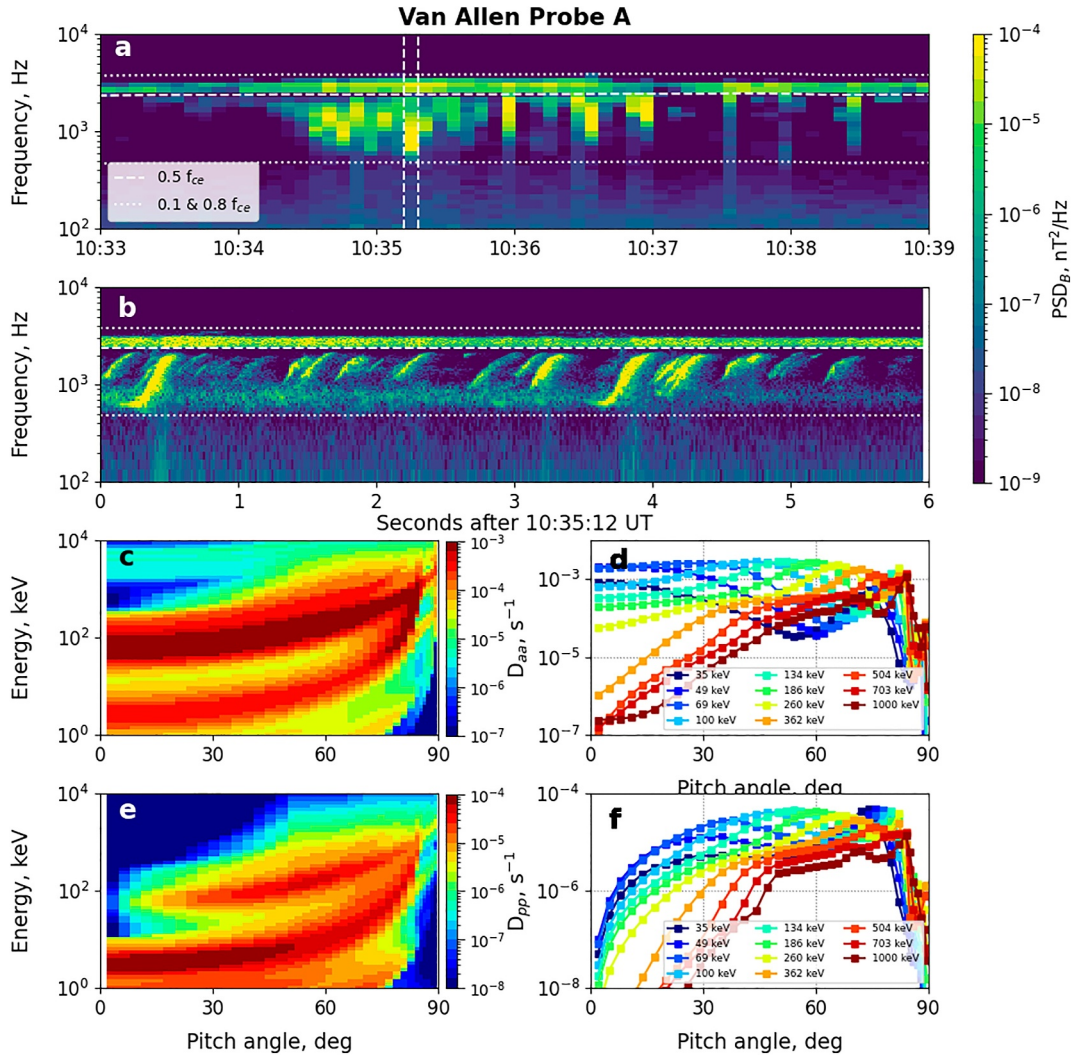

Figure 8. Similar to Figure 7, but for Van Allen Probe A.

upper band. The diffusion coefficients show similar features as for Van Allen Probe B (shown in Figure 7), that is, for electrons with energies <∼100 keV, there is strong pitch angle diffusion at lower pitch angles and strong energy diffusion at ∼45°. For electrons having energies in the range of ∼100–300 keV, pitch angle diffusion is stronger at higher pitch angles and energy diffusion is strongest at ∼60°–70°. For electrons having energies >∼300 keV, the pitch angle diffusion is comparatively weak, while the energy diffusion is weak at lower pitch angles but is stronger at larger pitch angles.

The diffusion coefficient results shown in Figures 7 and 8 are consistent with and appear to explain the observed flux variations presented in Figures 4 and 5. Quasilinear diffusion manifests as particles scattering along the resonance curves as defined by the resonance condition (Kennel & Petschek, 1966; Summers et al., 1998). Particles will scatter in directions of both increasing and decreasing energy and pitch angle. However, the net effect of this scattering is determined by the gradients of the underlying distribution function (Gendrin, 1981). Ultimately, the net effect of the diffusion is to move particles such that gradients in velocity space are reduced wherever possible. Regarding anisotropic distribution functions and whistler mode waves, the general rule of thumb is that the anisotropy of the distribution function decreases as the wave amplitude grows, via a natural self-limiting process (Allanson et al., 2021; Davidson et al., 1972; Ossakow et al., 1972; Ratcliffe & Watt, 2017; Tao et al., 2017). For electrons having energies <∼100 keV, strong pitch angle diffusion at lower pitch angles would thus result in steeper pitch angle distributions with enhanced anisotropy, and with higher losses at lower pitch angles, which do not reach the higher pitch angles at the core of the distribution. Conversely, for electrons within

the energy range of ∼100–300 keV, as pitch angle diffusion is stronger at larger pitch angles, this would result in a broadening of the pitch angle distribution with reduced anisotropy. For electrons having energy >300 keV, the pitch angle diffusion is significantly weak at pitch angles close to the loss cone. Thus, although the energy diffusion is also not very strong, the cumulative impact of both pitch angle and energy diffusion results in an overall flux enhancement at these energies. In addition, as the injected electron cloud drifts past Van Allen Probe B, which is closer to midnight, it results in a reduction in the measured electron fluxes at these energies. The drifted electron cloud gets further enhanced by the action of energy diffusion, which is measured as flux enhancement by Van Allen Probe A, which is closer to dawn. Here, we would like to add that it is well known from past studies that the outer radiation belt electron fluxes at greater than hundreds of keV exhibit a negative radial gradient, with fluxes decreasing radially outward. Therefore, as Van Allen Probe B was on an outbound orbit and Van Allen Probe A was on an inbound orbit, it might have also contributed to the observed flux variations in addition to the local interactions with chorus waves, resulting in electron fluxes at >300 keV decreasing at Van Allen Probe B and increasing at Van Allen Probe A. However, despite this, the overall estimates of the quasi-linear diffusion coefficients appear to be consistent with the measured flux variations, as presented in Figures 4 and 5.

To further corroborate the conclusion, which is based on data from only limited period in Figures 7 and 8, we calculated the pitch angle and momentum diffusion coefficients based on the observed wave power for the entire 1-hr time interval from 1030 to 1130 UT (as shown in the Figures S1 and S2 of Supporting Information S1). Figure S1 in Supporting Information S1 shows that pitch angle diffusion is strong and persistent during the entire 1-hr period along the trajectory of Van Allen Probe B, while for Van Allen Probe A, the pitch angle diffusion is stronger initially but gradually decreases with time. Figure S2 in Supporting Information S1 shows that the overall energy diffusion is weaker than pitch angle diffusion by more than an order of magnitude along the trajectory of both the Van Allen Probes during the entire 1-hr period. As Van Allen Probe B was close to the midnight, and Van Allen Probe A closer to dawn, this suggests that the electrons that were injected into the inner magnetosphere were in resonance with the intense chorus waves and experienced strong persistent pitch angle diffusion along their drift trajectory. The results therefore highlight the efficacy of intense chorus waves in driving strong rapid pitch angle diffusion and loss on very short timescales (∼10s of minutes).

Whilst the results appear to be consistent with the pitch angle diffusive dynamics in the quasi-linear regime, it is also worth considering whether there could be wave-particle interactions which are in the nonlinear regime. There are three main methods to determine whether the wave-particle interactions could fall into the nonlinear regime. The first method is best applied to the survey mode data and is performed by evaluating the quasilinear/nonlinear criteria as discussed in Karpman (1974) and Allanson et al. (2024). This criterion has been applied to the solar wind and the plasma sheet by Tong et al. (2019) and L. Gao et al. (2022), respectively. However, this method would likely calculate a significant underestimate (or a lower bound) of the number of nonlinear interaction events, since the survey mode data both "smoothes out" the spectra and reduces the instantaneous wave amplitudes (see discussion in Tao et al. (2014) and Allanson et al. (2024)). The second method is to try and evaluate the nonlinear inhomogeneity parameter (Albert et al., 2012; Bortnik et al., 2008; Omura et al., 2008), and this is best applied to burst mode data, since one requires the parameters defining individual chorus rising/falling tones. This method has been applied to chorus waves in the Van Allen Probe and THEMIS data sets in the inner magnetosphere by Zhang et al. (2019). The third method would be to take electromagnetic field waveform measurements from the spacecraft, and to evolve test-particles trajectories (e.g., as done by Gan et al. (2020)). All these methods could be an interesting basis for future study but are significant undertakings and are beyond the scope of this current work. However, we can use indicative approximations as discussed in Zhang et al. (2018) and Mourenas et al. (2018), which relate to the problem that we discuss, and give an approximate threshold for nonlinear interactions for wave amplitude of the order 150 pT or wave power of the order of 2.25×10^{-2} nT^2. Figures 6e and 6k show that during the 1-hr interval from 1030 to 1130 UT, the chorus wave power at both the Van Allen Probes exceeded this threshold multiple times (the dashed horizontal lines in Figures 6e and 6j), along with the ratio of wave amplitude to the background magnetic field (Figures 6f and 6l) exceeding the value of 10^{-3}. This indicates that there may be multiple instances of nonlinear interactions between the intense chorus waves and the injected electrons, which might have resulted in the rapid loss of electrons from the outer radiation belt. Additionally, we note recent progress on the general problem of particle diffusion due to cyclotron interactions with field-aligned R-/L-polarized waves. Cai et al. (2020) verified a semi-analytical approach that included the effects of resonant and near-resonant (resonance broadening) interactions in particle scattering. This resonance

broadening formula was then derived in Allanson et al. (2022) to exactly include the time-dependent contributions of non-resonant waves to diffusion. These effects generalize the results of the standard quasilinear theory, because quasilinear theory assumes contributions from particles that are in exact resonance only (Kennel & Engelmann, 1966). Further important developments were made by Yu et al. (2025) to calculate the departure time, demonstrated to be resulting from second-order processes. Yu et al. (2025) implemented the crucial departure time results in the formulas of Allanson et al. (2022), and then successfully verified them against the same test-particle simulations that were performed by Cai et al. (2020). The body of work provided by Cai et al. (2020); Allanson et al. (2022) and Yu et al. (2025), therefore, presents a complete and readily applicable resonance broadening theory for field-aligned R-/L-mode waves. We expect that these new results may provide additional information regarding diffusion near 90° pitch angles, for example, However, this is left to future work.

6. Conclusions

In this work, we used a conjunction between Van Allen Probe B, Van Allen Probe A and Arase to study the electron dynamics along an electron injection path in the Earth's outer radiation belt during two injection events during a moderate geomagnetic storm on 20 April 2018. During this event, Van Allen Probe B was closer to midnight, Van Allen Probe A was closer to dawn, and Arase was in the pre-noon sector. All three satellites were within a similar L-shell range, therefore providing a fortuitous conjunction with which to study the characteristics of wave-particle interactions of electrons along their drift trajectories on sub-drift timescales. We used both electron flux and electromagnetic wave measurements from the three spacecraft to characterize the observed flux variations, and to examine the observed dynamics in energy, L-shell, and MLT. We further calculated the pitch angle, momentum, and cross-term diffusion coefficients using a quasilinear approach and compared the results to the observed flux dynamics. The major findings from this study can be summarized as follows:

1. The 90° electron flux increased by several orders of magnitude across a wide range of energies after the injection events. Van Allen Probe B, which was close to midnight, observed the injections as dispersionless events, while Van Allen Probe A and Arase which were close to dawn and in the pre-noon sector, respectively, observed the injections as energy dispersed events, in agreement with the expected energy-dependent drift trajectories of injected electrons (c.f. Figure 3).
2. After the sudden increase in flux following the injection events, the 90° flux of $<\sim$100 keV electrons remained almost constant for a prolonged period along the trajectory of all three spacecraft. At mid-energies ($\sim$100–300 keV), the fluxes initially increased, followed by a gradual decrease. At high energies ($>\sim$300 keV), the fluxes decreased along the orbit of Van Allen Probe B, while increased along the orbits of Van Allen Probe A and Arase (c.f. Figures 3 and 4).
3. Between 1030 UT and 1130 UT, Van Allen Probe B and Van Allen Probe A were within the same L-shell range, between 5 and 6, and close to the midnight and dawn local time sectors, respectively. During this interval, the pitch angle distributions (PADs) of $<\sim$100 keV electrons became more 90°-peaked with increased anisotropy, while the PADs of $>\sim$100 keV electrons became broad with reduced anisotropy (c.f. Figure 5).
4. During this 1-hr interval from 1030 to 1130 UT, intense chorus waves with wave power $>10^{-4}$ nT^2 were observed along the trajectory of both Van Allen Probe B and Van Allen Probe A (c.f. Figure 6).
5. Calculation of pitch angle diffusion coefficients showed that pitch angle diffusion is only strong at lower pitch angles for $<\sim$100 keV electrons but has effects at larger pitch angles for $\sim$100–300 keV electrons, while for $>\sim$300 keV electrons, the pitch angle diffusion is generally weak at all pitch angles. Strong pitch angle diffusion results in a reduction in electron flux at pitch angles close to which the electrons are in resonance with the waves. Thus, these quasi-linear pitch angle diffusion coefficients, derived from observed wave parameters are consistent with the observed energy dependent electron flux variations. Interestingly, whilst being expected to experience only weak pitch angle diffusion, the calculated energy diffusion is also large, however, only for the higher energy $>\sim$300 keV electrons. This is consistent with the action of chorus-driven energy diffusion and an enhancement in the flux at these energies as a function of time observed at both Van Allen Probe A and Arase (c.f. Figures 7 and 8).

The results presented in this paper have two significant implications in radiation belt research. First, it shows that intense chorus waves can drive strong, rapid pitch angle diffusion on timescales of the order of tens of minutes. This is consistent with the recent findings by Olifer et al. (2024). Olifer et al. (2024) used data from the constellation of Global Positioning System (GPS) satellites to study the electron dynamics during an acceleration

event on 26 August 2018. Olifer et al. (2024) reported that during one of the electron burst events, chorus-driven local acceleration resulted in an order of magnitude increase in the measured flux on timescales of ∼20 min. In most of the radiation belt models, statistically averaged wave power is used as input, which leads to an underestimation of the large amplitude waves that, in turn, can result in disagreements between the model output electron flux/PSD and observation. These results thus highlight that in the future, these large amplitude waves need to be incorporated in the models as they have a significant impact on the fast radiation belt electron dynamics. Second, in situ measurements can provide observations only at a specific location at a specific time and thus lack the ability to provide a global overview of system. A solution to such a limitation is to use multi-spacecraft observations. In this work, we used a similar approach that helped us to gain a better understanding of the outer radiation belt electron dynamics. Here, we want to add that as in situ spacecraft observations provide point measurements, thus even using multi-spacecraft observations can not completely rule out the possibility of magnetospheric processes occurring at other local time sectors influencing the electron dynamics at the location of the spacecraft. However, our study showcases the advantage of using measurements from multiple spacecraft over single point measurements and can be used to plan future space missions with a constellation of spacecraft capable of providing simultaneous observations at different MLTs at a particular time.

Data Availability Statement

The Van Allen Probe data (both from ECT and EMFISIS instruments) used for this study are publicly available at RBSP-ECT (2019) and RBSP-EMFISIS (2019). The Arase electron flux data used for this study are available at the ERG Science Centre operated by ISAS/JAXA and ISEE/Nagoya University (Miyoshi et al., 2018). The solar wind parameters and geomagnetic indices data used in this study are publicly available at the website https://omniweb.gsfc.nasa.gov/form/omni_min.html, and also in Papitashvili and King (2020). The GOES 15 electron flux data used in this study is publicly available at https://www.ngdc.noaa.gov/stp/satellite/goes/dataaccess.html. Burst-mode power spectral densities were calculated using the methods described in this manuscript, using the publicly available EMFISIS data set and calibration coefficients, respectively. All of this is thoroughly described in the manuscript. The diffusion coefficients are calculated using a precomputed lookup table described in Hua et al. (2022) and has been discussed in the text.

Acknowledgments
SC, IJR and CEJW are all supported in part by STFC Grants ST/V006320/1, ST/X001008/1 and ST/W000369/1, and NERC Grants NE/V002554/2, NE/P017185/2 and NE/V0002759/2. IRM is supported by a Discovery Grant from Canadian NSERC. LO is supported by a Banting Post-Doctoral Fellowship. LGO is partially supported by the Canadian Space Agency. OA acknowledges financial support from the University of Birmingham, the University of Exeter, and the UK Research and Innovation (UKRI) Natural Environment Research Council (NERC) Independent Research Fellowship NE/V013963/1 and NE/V013963/2. RB acknowledges UKRI NERC GW4+ DTP2 studentship project (4253) 2697077.

References

Agapitov, O. V., Artemyev, A. V., Mourenas, D., Mozer, F. S., & Krasnoselskikh, V. (2015). Nonlinear local parallel acceleration of electrons through Landau trapping by oblique whistler mode waves in the outer radiation belt. *Geophysical Research Letters*, *42*(23), 10140–10149. https://doi.org/10.1002/2015GL066887

Albert, J. M. (2005). Evaluation of quasi-linear diffusion coefficients for whistler mode waves in a plasma with arbitrary density ratio. *Journal of Geophysical Research*, *110*(A3). https://doi.org/10.1029/2004JA010844

Albert, J. M. (2010). Diffusion by one wave and by many waves. *Journal of Geophysical Research*, *115*(A3). https://doi.org/10.1029/2009JA014732

Albert, J. M., Starks, M. J., Horne, R. B., Meredith, N. P., & Glauert, S. A. (2016). Quasi-linear simulations of inner radiation belt electron pitch angle and energy distributions. *Geophysical Research Letters*, *43*(6), 2381–2388. https://doi.org/10.1002/2016GL067938

Albert, J. M., Tao, X., & Bortnik, J. (2012). Aspects of nonlinear wave-particle interactions. In *Dynamics of the earth's radiation belts and inner magnetosphere* (pp. 255–264). American Geophysical Union (AGU). https://doi.org/10.1029/2012GM001324

Allanson, O., Elsden, T., Watt, C., & Neukirch, T. (2022). Weak turbulence and quasilinear diffusion for relativistic wave-particle interactions via a Markov approach. *Frontiers in Astronomy and Space Sciences, Volume 8, 2021*, *8*. https://doi.org/10.3389/fspas.2021.805699

Allanson, O., Ma, D., Osmane, A., Albert, J. M., Bortnik, J., Watt, C. E. J., et al. (2024). The challenge to understand the zoo of particle transport regimes during resonant wave-particle interactions for given survey-mode wave spectra. *Frontiers in Astronomy and Space Sciences, Volume 11, 2024*, *11*. https://doi.org/10.3389/fspas.2024.1332931

Allanson, O., Watt, C. E. J., Allison, H. J., & Ratcliffe, H. (2021). Electron diffusion and advection during nonlinear interactions with whistler-mode waves. *Journal of Geophysical Research: Space Physics*, *126*(5), e2020JA028793. https://doi.org/10.1029/2020JA028793

Allanson, O., Watt, C. E. J., Ratcliffe, H., Allison, H. J., Meredith, N. P., Bentley, S. N., et al. (2020). Particle-in-Cell experiments examine electron diffusion by whistler-mode waves: 2. Quasi-linear and nonlinear dynamics. *Journal of Geophysical Research: Space Physics*, *125*(7), e2020JA027949. https://doi.org/10.1029/2020JA027949

Artemyev, A., Agapitov, O., Mourenas, D., Krasnoselskikh, V., Shastun, V., & Mozer, F. (2016). Oblique whistler-mode waves in the Earth's inner magnetosphere: Energy distribution, origins, and role in radiation belt dynamics. *Space Science Reviews*, *200*(1), 261–355. https://doi.org/10.1007/s11214-016-0252-5

Baker, D. N., Kanekal, S. G., & Blake, J. B. (2004). Characterizing the Earth's outer Van Allen zone using a radiation belt content index. *Space Weather*, *2*(2). https://doi.org/10.1029/2003SW000026

Baker, D. N., Kanekal, S. G., Hoxie, V. C., Batiste, S., Bolton, M., Li, X., et al. (2013). The Relativistic Electron-Proton Telescope (REPT) instrument on board the Radiation Belt Storm Probes (RBSP) spacecraft: Characterization of Earth's radiation belt high-energy particle populations. *Space Science Reviews*, *179*(1), 337–381. https://doi.org/10.1007/s11214-012-9950-9

Bingham, S. T., Mouikis, C. G., Kistler, L. M., Boyd, A. J., Paulson, K., Farrugia, C. J., et al. (2018). The outer radiation belt response to the storm time development of seed electrons and chorus wave activity during CME and CIR driven storms. *Journal of Geophysical Research: Space Physics*, *123*(12), 10139–10157. https://doi.org/10.1029/2018JA025963

Blake, J. B., Carranza, P. A., Claudepierre, S. G., Clemmons, J. H., Crain, W. R., Jr., Dotan, Y., et al. (2013). The Magnetic Electron Ion Spectrometer (MagEIS) instruments aboard the Radiation Belt Storm Probes (RBSP) spacecraft. *Space Science Reviews*, *179*(1–4), 383–421. https://doi.org/10.1007/s11214-013-9991-8

Bortnik, J., Thorne, R. M., & Inan, U. S. (2008). Nonlinear interaction of energetic electrons with large amplitude chorus. *Geophysical Research Letters*, *35*(21). https://doi.org/10.1029/2008GL035500

Breneman, A., Cattell, C., Wygant, J., Kersten, K., Wilson, L. B., III., Schreiner, S., et al. (2011). Large-amplitude transmitter-associated and lightning-associated whistler waves in the Earth's inner plasmasphere at L < 2. *Journal of Geophysical Research: Space Physics*, *116*(A6). https://doi.org/10.1029/2010JA016288

Cai, B., Wu, Y., & Tao, X. (2020). Effects of nonlinear resonance broadening on interactions between electrons and whistler mode waves. *Geophysical Research Letters*, *47*(11). https://doi.org/10.1029/2020GL087991

Camporeale, E. (2015). Resonant and nonresonant whistlers-particle interaction in the radiation belts. *Geophysical Research Letters*, *42*(9), 3114–3121. https://doi.org/10.1002/2015GL063874

Capannolo, L., Marshall, R., Li, W., Berland, G., Duderstadt, K., Sivadas, N., et al. (2024). Unraveling the atmospheric energy input and ionization due to EMIC-driven electron precipitation from ELFIN observations. *AGU Advances*, *5*(3), e2023AV001096. https://doi.org/10.1029/2023AV001096

Chakraborty, S., Mann, I. R., Watt, C. E. J., Rae, I. J., Olifer, L., Ozeke, L. G., et al. (2022). Intense chorus waves are the cause of Flux-limiting in the heart of the outer radiation belt. *Scientific Reports*, *12*(1), 21717. https://doi.org/10.1038/s41598-022-26189-9

Chakraborty, S., Rae, I. J., Killey, S., Ojha, B., Watt, C. E. J., Potts, C., et al. (2024). Statistical survey of pitch angle anisotropy of relativistic electrons in the outer radiation belt and its variation with solar wind/geomagnetic activity. *Frontiers in Astronomy and Space Sciences*, *11*. https://doi.org/10.3389/fspas.2024.1474503

Claudepierre, S. G., Ma, Q., Bortnik, J., O'Brien, T. P., Fennell, J. F., & Blake, J. B. (2020). Empirically estimated electron lifetimes in the Earth's radiation belts: Comparison with theory. *Geophysical Research Letters*, *47*(3), e2019GL086056. https://doi.org/10.1029/2019GL086056

Colpitts, C., Miyoshi, Y., Kasahara, Y., Delzanno, G. L., Wygant, J. R., Cattell, C. A., et al. (2020). First direct observations of propagation of discrete Chorus elements from the equatorial source to higher latitudes, using the Van Allen Probes and Arase satellites. *Journal of Geophysical Research: Space Physics*, *125*(10), e2020JA028315. https://doi.org/10.1029/2020JA028315

Cully, C. M., Bonnell, J. W., & Ergun, R. E. (2008). THEMIS observations of long-lived regions of large-amplitude whistler waves in the inner magnetosphere. *Geophysical Research Letters*, *35*(17). https://doi.org/10.1029/2008GL033643

Davidson, R. C., Hammer, D. A., Haber, I., & Wagner, C. E. (1972). Nonlinear development of electromagnetic instabilities in anisotropic plasmas. *The Physics of Fluids*, *15*(2), 317–333. https://doi.org/10.1063/1.1693910

Drozdov, A. Y., Allison, H. J., Shprits, Y. Y., Usanova, M., Saikin, A., & Wang, D. (2022). Depletions of multi-MeV electrons and their association to minima in phase space density. *Geophysical Research Letters*, *49*(8), e2021GL097620. https://doi.org/10.1029/2021GL097620

Duderstadt, K. A., Huang, C.-L., Spence, H. E., Smith, S., Blake, J. B., Crew, A. B., et al. (2021). Estimating the impacts of radiation belt electrons on atmospheric chemistry using FIREBIRD II and Van Allen Probes observations. *Journal of Geophysical Research: Atmospheres*, *126*(7), e2020JD033098. https://doi.org/10.1029/2020JD033098

Elkington, S. R., Hudson, M. K., & Chan, A. A. (1999). Acceleration of relativistic electrons via drift-resonant interaction with toroidal-mode Pc-5 ULF oscillations. *Geophysical Research Letters*, *26*(21), 3273–3276. https://doi.org/10.1029/1999GL003659

Elkington, S. R., Hudson, M. K., & Chan, A. A. (2003). Resonant acceleration and diffusion of outer zone electrons in an asymmetric geomagnetic field. *Journal of Geophysical Research: Space Physics*, *108*(A3). https://doi.org/10.1029/2001JA009202

Fälthammar, C.-G. (1965). Effects of time-dependent electric fields on geomagnetically trapped radiation. *Journal of Geophysical Research (1896–1977)*, *70*(11), 2503–2516. https://doi.org/10.1029/JZ070i011p02503

Foster, J. C., Erickson, P. J., Omura, Y., Baker, D. N., Kletzing, C. A., & Claudepierre, S. G. (2017). Van Allen Probes observations of prompt MeV radiation belt electron acceleration in nonlinear interactions with VLF chorus. *Journal of Geophysical Research: Space Physics*, *122*(1), 324–339. https://doi.org/10.1002/2016JA023429

Gan, L., Li, W., Ma, Q., Albert, J. M., Artemyev, A. V., & Bortnik, J. (2020). Nonlinear interactions between radiation belt electrons and chorus waves: Dependence on wave amplitude modulation. *Geophysical Research Letters*, *47*(4), e2019GL085987. https://doi.org/10.1029/2019GL085987

Ganushkina, N. Y., Swiger, B., Dubyagin, S., Matéo-Vélez, J.-C., Liemohn, M. W., Sicard, A., & Payan, D. (2021). Worst-case severe environments for surface charging observed at LANL satellites as dependent on solar wind and geomagnetic conditions. *Space Weather*, *19*(9), e2021SW002732. https://doi.org/10.1029/2021SW002732

Gao, L., Vainchtein, D., Artemyev, A. V., & Zhang, X.-J. (2022a). Statistics of whistler-mode waves in the near-Earth plasma sheet. *Journal of Geophysical Research: Space Physics*, *127*(8), e2022JA030603. https://doi.org/10.1029/2022JA030603

Gao, X., Chen, R., Lu, Q., Chen, L., Chen, H., & Wang, X. (2022b). Observational evidence for the origin of repetitive chorus emissions. *Geophysical Research Letters*, *49*(12), e2022GL099000. https://doi.org/10.1029/2022GL099000

Gao, X., Lu, Q., Kang, N., Ke, Y., Ma, J., Tsurutani, B., et al. (2022c). Study on source region and generation mechanism of oblique whistler-mode waves in the Earth's magnetosphere. *Journal of Geophysical Research: Space Physics*, *127*(9), e2022JA030804. https://doi.org/10.1029/2022JA030804

Gendrin, R. (1981). General relationships between wave amplification and particle diffusion in a magnetoplasma. *Reviews of Geophysics*, *19*(1), 171–184. https://doi.org/10.1029/RG019i001p00171

Glauert, S. A., & Horne, R. B. (2005). Calculation of pitch angle and energy diffusion coefficients with the PADIE code. *Journal of Geophysical Research: Space Physics*, *110*(A4). https://doi.org/10.1029/2004JA010851

Hartley, D. P., Chen, Y., Kletzing, C. A., Denton, M. H., & Kurth, W. S. (2015). Applying the cold plasma dispersion relation to whistler mode chorus waves: EMFISIS wave measurements from the Van Allen Probes. *Journal of Geophysical Research: Space Physics*, *120*(2), 1144–1152. https://doi.org/10.1002/2014JA020808

Hartley, D. P., Christopher, I. W., Kletzing, C. A., Kurth, W. S., Santolik, O., Kolmasova, I., et al. (2023). Chorus wave properties from Van Allen Probes: Quantifying the impact of the sheath corrected electric field. *Geophysical Research Letters*, *50*(7), e2023GL102922. https://doi.org/10.1029/2023GL102922

Hartley, D. P., Kletzing, C. A., Chen, L., Horne, R. B., & Santolík, O. (2019). Van Allen Probes observations of chorus wave vector orientations: Implications for the chorus-to-hiss mechanism. *Geophysical Research Letters*, *46*(5), 2337–2346. https://doi.org/10.1029/2019GL082111

Hartley, D. P., Kletzing, C. A., Kurth, W. S., Bounds, S. R., Averkamp, T. F., Hospodarsky, G. B., et al. (2016). Using the cold plasma dispersion relation and whistler mode waves to quantify the antenna sheath impedance of the Van Allen Probes EFW instrument. *Journal of Geophysical Research: Space Physics*, *121*(5), 4590–4606. https://doi.org/10.1002/2016JA022501

Higashio, N., Takashima, T., Shinohara, I., & Matsumoto, H. (2018). The extremely high-energy electron experiment (XEP) onboard the Arase (ERG) satellite. *Earth Planets and Space*, *70*(1), 134. https://doi.org/10.1186/s40623-018-0901-x

Horne, R. B., & Thorne, R. M. (1998). Potential waves for relativistic electron scattering and stochastic acceleration during magnetic storms. *Geophysical Research Letters*, *25*(15), 3011–3014. https://doi.org/10.1029/98GL01002

Horne, R. B., Thorne, R. M., Shprits, Y. Y., Meredith, N. P., Glauert, S. A., Smith, A. J., et al. (2005). Wave acceleration of electrons in the Van Allen radiation belts. *Nature*, *437*(7056), 227–230. https://doi.org/10.1038/nature03939

Hua, M., Bortnik, J., Kellerman, A. C., Camporeale, E., & Ma, Q. (2022). Ensemble modeling of radiation belt electron flux decay following a geomagnetic storm: Dependence on key input parameters. *Space Weather*, *20*(8), e2022SW003051. https://doi.org/10.1029/2022SW003051

Hua, M., Bortnik, J., Kellerman, A. C., Camporeale, E., & Ma, Q. (2023a). Ensemble modeling of radiation belt electron acceleration by chorus waves: Dependence on key input parameters. *Space Weather*, *21*(3), e2022SW003234. https://doi.org/10.1029/2022SW003234

Hua, M., Bortnik, J., & Ma, D. (2023b). Dependence of electron flux dropouts in the Earth's outer radiation belt on energy and driving parameters during geomagnetic storms. *Journal of Geophysical Research: Space Physics*, *128*(10), e2023JA031882. https://doi.org/10.1029/2023JA031882

Hua, M., Li, W., Ni, B., Ma, Q., Green, A., Shen, X., et al. (2020). Very-Low-Frequency transmitters bifurcate energetic electron belt in near-earth space. *Nature Communications*, *11*(1), 4847. https://doi.org/10.1038/s41467-020-18545-y

Hudson, M., Elkington, S., Lyon, J., & Goodrich, C. (2000). Increase in relativistic electron flux in the inner magnetosphere: ULF wave mode structure. *Advances in Space Research*, *25*(12), 2327–2337. https://doi.org/10.1016/S0273-1177(99)00518-9

Hudson, M. K., Kress, B. T., Mueller, H.-R., Zastrow, J. A., & Bernard Blake, J. (2008). Relationship of the Van Allen radiation belts to solar wind drivers. *Journal of Atmospheric and Solar-Terrestrial Physics*, *70*(5), 708–729. https://doi.org/10.1016/j.jastp.2007.11.003

Jaynes, A. N., Ali, A. F., Elkington, S. R., Malaspina, D. M., Baker, D. N., Li, X., et al. (2018). Fast diffusion of ultrarelativistic electrons in the outer radiation belt: 17 March 2015 storm event. *Geophysical Research Letters*, *45*(20), 10874–10882. https://doi.org/10.1029/2018GL079786

Kanekal, S., & Miyoshi, Y. (2021). Dynamics of the terrestrial radiation belts: A review of recent results during the VarSITI (variability of the Sun and its terrestrial impact) era, 2014–2018. *Progress in Earth and Planetary Science*, *8*(1), 35. https://doi.org/10.1186/s40645-021-00413-y

Karpman, V. I. (1974). Nonlinear effects in the ELF waves propagating along the magnetic field in the magnetosphere. *Space Science Reviews*, *16*(3). https://doi.org/10.1007/BF00171564

Kellogg, P. J., Cattell, C. A., Goetz, K., Monson, S. J., & Wilson, L. B., III. (2011). Large amplitude whistlers in the magnetosphere observed with Wind-Waves. *Journal of Geophysical Research: Space Physics*, *116*(A9). https://doi.org/10.1029/2010JA015919

Kennel, C. F., & Engelmann, F. (1966). Velocity space diffusion from weak plasma turbulence in a magnetic field. *The Physics of Fluids*, *9*(12), 2377–2388. https://doi.org/10.1063/1.1761629

Kennel, C. F., & Petschek, H. E. (1966). Limit on stably trapped particle fluxes. *Journal of Geophysical Research (1896–1977)*, *71*(1), 1–28. https://doi.org/10.1029/JZ071i001p00001

Kletzing, C., Bortnik, J., Hospodarsky, G., Kurth, W., Santolik, O., Smitth, C., et al. (2023). The Electric and Magnetic Fields Instrument Suite and Integrated Science (EMFISIS): Science, data, and usage best practices. *Space Science Reviews*, *219*(4), 28. https://doi.org/10.1007/s11214-023-00973-z

Kletzing, C. A., Kurth, W. S., Acuna, M., MacDowall, R. J., Torbert, R. B., Averkamp, T., et al. (2013). The Electric and Magnetic Field Instrument Suite and Integrated Science (EMFISIS) on RBSP. *Space Science Reviews*, *179*(1–4), 127–181. https://doi.org/10.1007/s11214-013-9993-6

Kondrashov, D., Drozdov, A. Y., & Shprits, Y. (2024). Nonlinear wave-particle interaction effects on radiation belt electron dynamics in 9 October 2012 storm. *Journal of Geophysical Research: Space Physics*, *129*(9), e2024JA032898. https://doi.org/10.1029/2024JA032898

Koons, H., & Roeder, J. (1990). A survey of equatorial magnetospheric wave activity between 5 and 8 RE. *Planetary and Space Science*, *38*(10), 1335–1341. https://doi.org/10.1016/0032-0633(90)90136-E

Kurita, S., Miyoshi, Y., Kasahara, S., Yokota, S., Kasahara, Y., Matsuda, S., et al. (2018). Deformation of electron pitch angle distributions caused by upper band chorus observed by the Arase satellite. *Geophysical Research Letters*, *45*(16), 7996–8004. https://doi.org/10.1029/2018GL079104

Lai, S. T., Cahoy, K., Lohmeyer, W., Carlton, A., Aniceto, R., & Minow, J. (2018). Chapter 16—deep dielectric charging and spacecraft anomalies. In N. Buzulukova (Ed.), *Extreme events in geospace* (pp. 419–432). Elsevier. https://doi.org/10.1016/B978-0-12-812700-1.00016-9

Lejosne, S., Allison, H. J., Blum, L. W., Drozdov, A. Y., Hartinger, M. D., Hudson, M. K., et al. (2022). Differentiating between the leading processes for electron radiation belt acceleration. *Frontiers in Astronomy and Space Sciences*, *9*. https://doi.org/10.3389/fspas.2022.896245

Lerche, I. (1968). Quasilinear theory of resonant diffusion in a Magneto-active, relativistic plasma. *The Physics of Fluids*, *11*(8), 1720–1727. https://doi.org/10.1063/1.1692186

Li, J., Bortnik, J., An, X., Li, W., Angelopoulos, V., Thorne, R. M., et al. (2019). Origin of two-band chorus in the radiation belt of Earth. *Nature Communications*, *10*(1), 4672. https://doi.org/10.1038/s41467-019-12561-3

Li, W., Bortnik, J., Thorne, R. M., & Angelopoulos, V. (2011). Global distribution of wave amplitudes and wave normal angles of chorus waves using THEMIS wave observations. *Journal of Geophysical Research: Space Physics*, *116*(A12). https://doi.org/10.1029/2011JA017035

Li, W., Mourenas, D., Artemyev, A. V., Agapitov, O. V., Bortnik, J., Albert, J. M., et al. (2014). Evidence of stronger pitch angle scattering loss caused by oblique whistler-mode waves as compared with quasi-parallel waves. *Geophysical Research Letters*, *41*(17), 6063–6070. https://doi.org/10.1002/2014GL061260

Li, Y., Yue, C., Liu, Y., Zong, Q.-G., Zou, H., & Ye, Y. (2023). Dynamics of the inner electron radiation belt: A review. *Earth and Planetary Physics*, *7*(1), 109–118. https://doi.org/10.26464/epp2023009

Malaspina, D. M., Zhu, H., & Drozdov, A. Y. (2020). A wave model and diffusion coefficients for plasmaspheric hiss parameterized by Plasmapause location. *Journal of Geophysical Research: Space Physics*, *125*(2), e2019JA027415. https://doi.org/10.1029/2019JA027415

Mann, I. R., Lee, E. A., Claudepierre, S. G., Fennell, J. F., Degeling, A., Rae, I. J., et al. (2013). Discovery of the action of a geophysical synchrotron in the Earth's Van Allen radiation belts. *Nature Communications*, *4*(1), 2795. https://doi.org/10.1038/ncomms3795

Mateo-Velez, J.-C., Sicard, A., Payan, D., Ganushkina, N., Meredith, N. P., & Sillanpäa, I. (2018). Spacecraft surface charging induced by severe environments at geosynchronous orbit. *Space Weather*, *16*(1), 89–106. https://doi.org/10.1002/2017SW001689

Millan, R. M., & Baker, D. N. (2012). Acceleration of particles to high energies in Earth's radiation belts. *Space Science Reviews*, *173*(1), 103–131. https://doi.org/10.1007/s11214-012-9941-x

Minow, J. I., Jordanova, V. K., Pitchford, D., Ganushkina, N. Y., Zheng, Y., Luca Delzanno, G., et al. (2024). ISWAT spacecraft surface charging review. *Advances in Space Research*. https://doi.org/10.1016/j.asr.2024.08.058

Miyoshi, Y., Hori, T., Shoji, M., Teramoto, M., Chang, T. F., Segawa, T., et al. (2018). The ERG Science Center. *Earth, Planets and Space*, *70*. https://doi.org/10.1186/s40623-018-0867-8

Miyoshi, Y., Shinohara, I., Ukhorskiy, S., Claudepierre, S. G., Mitani, T., Takashima, T., et al. (2022). Collaborative research activities of the Arase and Van Allen Probes. *Space Science Reviews*, *218*(5), 38. https://doi.org/10.1007/s11214-022-00885-4

Mourenas, D., Zhang, X.-J., Artemyev, A. V., Angelopoulos, V., Thorne, R. M., Bortnik, J., et al. (2018). Electron nonlinear resonant interaction with short and intense parallel chorus wave packets. *Journal of Geophysical Research: Space Physics*, *123*(6), 4979–4999. https://doi.org/10.1029/2018JA025417

Mozer, F. S., Agapitov, O. V., Blake, J. B., & Vasko, I. Y. (2018). Simultaneous observations of lower band chorus emissions at the equator and microburst precipitating electrons in the ionosphere. *Geophysical Research Letters*, *45*(2), 511–516. https://doi.org/10.1002/2017GL076120

Olifer, L., Morley, S. K., Ozeke, L. G., Mann, I. R., Kalliokoski, M. M. H., Henderson, M. G., et al. (2024). Rapid acceleration bursts in the Van Allen radiation belt. *Journal of Geophysical Research: Space Physics*, *129*(5), e2024JA032544. https://doi.org/10.1029/2024JA032544

Omura, Y., Katoh, Y., & Summers, D. (2008). Theory and simulation of the generation of whistler-mode chorus. *Journal of Geophysical Research: Space Physics*, *113*(A4). https://doi.org/10.1029/2007JA012622

Osmane, A., Kilpua, E., George, H., Allanson, O., & Kalliokoski, M. (2023). Radial transport in the Earth's radiation belts: Linear, quasi-linear, and higher-order processes. *The Astrophysical Journal—Supplement Series*, *269*(2), 44. https://doi.org/10.3847/1538-4365/acff6a

Osmane, A., Sandhu, J. K., Elsden, T., Allanson, O., & Turc, L. (2025). Radial diffusion driven by spatially localized ULF waves in the Earth's magnetosphere. *Journal of Geophysical Research: Space Physics*, *130*(3). https://doi.org/10.1029/2024JA033393

Ossakow, S. L., Ott, E., & Haber, I. (1972). Nonlinear evolution of whistler instabilities. *The Physics of Fluids*, *15*(12), 2314–2326. https://doi.org/10.1063/1.1693875

Ozaki, M., Shiokawa, K., Kataoka, R., Mlynczak, M., Paxton, L., Connors, M., et al. (2024). Localized mesospheric ozone destruction corresponding to isolated proton aurora coming from Earth's radiation belt. *Scientific Reports*, *12*(1), 16300. https://doi.org/10.1038/s41598-022-20548-2

Ozeke, L. G., Mann, I. R., Murphy, K. R., Jonathan Rae, I., & Milling, D. K. (2014a). Analytic expressions for ULF wave radiation belt radial diffusion coefficients. *Journal of Geophysical Research: Space Physics*, *119*(3), 1587–1605. https://doi.org/10.1002/2013JA019204

Ozeke, L. G., Mann, I. R., Murphy, K. R., Rae, I. J., Milling, D. K., Elkington, S. R., et al. (2012). ULF wave derived radiation belt radial diffusion coefficients. *Journal of Geophysical Research: Space Physics*, *117*(A4). https://doi.org/10.1029/2011JA017463

Ozeke, L. G., Mann, I. R., Olifer, L., Dufresne, K. Y., Morley, S. K., Claudepierre, S. G., et al. (2020). Rapid outer radiation belt flux dropouts and fast acceleration during the March 2015 and 2013 storms: The role of ultra-low frequency wave transport from a dynamic outer boundary. *Journal of Geophysical Research: Space Physics*, *125*(2). https://doi.org/10.1029/2019JA027179

Ozeke, L. G., Mann, I. R., Turner, D. L., Murphy, K. R., Degeling, A. W., Rae, I. J., & Milling, D. K. (2014b). Modeling cross L shell impacts of magnetopause shadowing and ULF wave radial diffusion in the Van Allen belts. *Geophysical Research Letters*, *41*(19), 6556–6562. https://doi.org/10.1002/2014GL060787

Papitashvili, N. E., & King, J. H. (2020). OMNI 5-min data set [Dataset]. *NASA Space Physics Data Facility*. https://doi.org/10.48322/gbpg-5r77

Paschmann, G., & Daly, P. W. (1998). *Analysis methods for multi-spacecraft data* (Vol. 1). ISSI Scientific Reports Series SR-001, ESA/ISSI.

Patel, M., Hudson, M., Kress, B., & Qin, M. (2025). Simulation of ULF wave modulated electron precipitation during the 17 March 2015 storm. *Journal of Geophysical Research: Space Physics*, *130*(2), e2024JA033115. https://doi.org/10.1029/2024JA033115

Rae, I. J., Murphy, K. R., Watt, C. E. J., Halford, A. J., Mann, I. R., Ozeke, L. G., et al. (2018). The role of localized compressional ultra-low frequency waves in energetic electron precipitation. *Journal of Geophysical Research: Space Physics*, *123*(3), 1900–1914. https://doi.org/10.1002/2017JA024674

Ratcliffe, H., & Watt, C. E. J. (2017). Self-consistent formation of a 0.5 cyclotron frequency gap in magnetospheric whistler mode waves. *Journal of Geophysical Research: Space Physics*, *122*(8), 8166–8180. https://doi.org/10.1002/2017JA024399

RBSP-ECT. (2019). LANL RBSP-ECT online data repository [Dataset]. *RBSP ECT*. Retrieved from https://rbsp-ect.newmexicoconsortium.org/data_pub/rbspa/ECT/level3/

RBSP-EMFISIS. (2019). UIOWA RBSP-EMFISIS online data repository [Dataset]. *RBSP EMFISIS*. Retrieved from https://emfisis.physics.uiowa.edu/data/L2_products

Reeves, G. D., McAdams, K. L., Friedel, R. H. W., & O'Brien, T. P. (2003). Acceleration and loss of relativistic electrons during geomagnetic storms. *Geophysical Research Letters*, *30*(10). https://doi.org/10.1029/2002GL016513

Ripoll, J.-F., Claudepierre, S. G., Ukhorskiy, A. Y., Colpitts, C., Li, X., Fennell, J. F., & Crabtree, C. (2020). Particle dynamics in the Earth's radiation belts: Review of current research and open questions. *Journal of Geophysical Research: Space Physics*, *125*(5), e2019JA026735. https://doi.org/10.1029/2019JA026735

Ripoll, J.-F., Santolík, O., Reeves, G. D., Kurth, W. S., Denton, M. H., Loridan, V., et al. (2017). Effects of whistler mode hiss waves in March 2013. *Journal of Geophysical Research: Space Physics*, *122*(7), 7433–7462. https://doi.org/10.1002/2017JA024139

Ripoll, J.-F., Thaller, S. A., Hartley, D. P., Cunningham, G. S., Pierrard, V., Kurth, W. S., et al. (2022). Statistics and empirical models of the plasmasphere boundaries from the Van Allen Probes for radiation belt physics. *Geophysical Research Letters*, *49*(21), e2022GL101402. https://doi.org/10.1029/2022GL101402

Rodger, C. J., Clilverd, M. A., Seppälä, A., Thomson, N. R., Gamble, R. J., Parrot, M., et al. (2010). Radiation belt electron precipitation due to geomagnetic storms: Significance to middle atmosphere Ozone chemistry. *Journal of Geophysical Research: Space Physics*, *115*(A11). https://doi.org/10.1029/2010JA015599

Ross, J. P. J., Glauert, S. A., Horne, R. B., Watt, C. E. J., & Meredith, N. P. (2021). On the variability of EMIC waves and the consequences for the relativistic electron radiation belt population. *Journal of Geophysical Research: Space Physics*, *126*(12), e2021JA029754. https://doi.org/10.1029/2021JA029754

Saito, S., Kurita, S., Miyoshi, Y., Kasahara, S., Yokota, S., Keika, K., et al. (2021). Data-driven simulation of rapid flux enhancement of energetic electrons with an upper-band whistler burst. *Journal of Geophysical Research: Space Physics*, *126*(4), e2020JA028979. https://doi.org/10.1029/2020JA028979

Santolík, O., Kletzing, C. A., Kurth, W. S., Hospodarsky, G. B., & Bounds, S. R. (2014). Fine structure of large-amplitude chorus wave packets. *Geophysical Research Letters*, *41*(2), 293–299. https://doi.org/10.1002/2013GL058889

Santolík, O., Miyoshi, Y., Kolmašová, I., Matsuda, S., Hospodarsky, G. B., Hartley, D. P., et al. (2021). Inter-calibrated measurements of intense whistlers by Arase and Van Allen Probes. *Journal of Geophysical Research: Space Physics*, *126*(9), e2021JA029700. https://doi.org/10.1029/2021JA029700

Santolík, O., Parrot, M., & Lefeuvre, F. (2003). Singular value decomposition methods for wave propagation analysis. *Radio Science*, *38*(1). https://doi.org/10.1029/2000RS002523

Santolík, O., Pickett, J. S., Gurnett, D. A., & Storey, L. R. O. (2002). Magnetic component of narrowband ion cyclotron waves in the auroral zone. *Journal of Geophysical Research*, *107*(A12), 17. https://doi.org/10.1029/2001JA000146

Shang, X., Liu, S., Chen, L., Gao, Z., Wang, G., He, Q., et al. (2021). ULF-modulation of whistler-mode waves in the inner magnetosphere during solar wind compression. *Journal of Geophysical Research: Space Physics*, *126*(8), e2021JA029353. https://doi.org/10.1029/2021JA029353

Shprits, Y. Y., Drozdov, A. Y., Spasojevic, M., Kellerman, A. C., Usanova, M. E., Engebretson, M. J., et al. (2016). Wave-induced loss of ultra-relativistic electrons in the Van Allen radiation belts. *Nature Communications*, *7*(1), 12883. https://doi.org/10.1038/ncomms12883

Shumko, M., Turner, D. L., O'Brien, T. P., Claudepierre, S. G., Sample, J., Hartley, D. P., et al. (2018). Evidence of microbursts observed near the equatorial plane in the outer Van Allen radiation belt. *Geophysical Research Letters*, *45*(16), 8044–8053. https://doi.org/10.1029/2018GL078451

Spence, H. E., Reeves, G. D., Baker, D. N., Blake, J. B., Bolton, M., Bourdarie, S., et al. (2013). Science goals and overview of the Radiation Belt Storm Probes (RBSP) Energetic particle, Composition, and Thermal plasma (ECT) suite on NASA's Van Allen Probes mission. *Space Science Reviews*, *179*(1–4), 311–336. https://doi.org/10.1007/s11214-013-0007-5

Summers, D. (2005). Quasi-linear diffusion coefficients for field-aligned electromagnetic waves with applications to the magnetosphere. *Journal of Geophysical Research: Space Physics*, *110*(A8). https://doi.org/10.1029/2005JA011159

Summers, D., Ma, C., & Mukai, T. (2004). Competition between acceleration and loss mechanisms of relativistic electrons during geomagnetic storms. *Journal of Geophysical Research: Space Physics*, *109*(A4). https://doi.org/10.1029/2004JA010437

Summers, D., Thorne, R. M., & Xiao, F. (1998). Relativistic theory of wave-particle resonant diffusion with application to electron acceleration in the magnetosphere. *Journal of Geophysical Research*, *103*(A9), 20487–20500. https://doi.org/10.1029/98JA01740

Tao, X., Bortnik, J., Albert, J. M., Thorne, R. M., & Li, W. (2014). Effects of discreteness of chorus waves on quasilinear diffusion-based modeling of energetic electron dynamics. *Journal of Geophysical Research: Space Physics*, *119*(11), 8848–8857. https://doi.org/10.1002/2014JA020022

Tao, X., Chen, L., Liu, X., Lu, Q., & Wang, S. (2017). Quasilinear analysis of saturation properties of broadband whistler mode waves. *Geophysical Research Letters*, *44*(16), 8122–8129. https://doi.org/10.1002/2017GL074881

Teng, S., Tao, X., & Li, W. (2019). Typical characteristics of whistler mode waves categorized by their spectral properties using Van Allen Probes observations. *Geophysical Research Letters*, *46*(7), 3607–3614. https://doi.org/10.1029/2019GL082161

Thorne, R. M. (1977). Energetic radiation belt electron precipitation: A natural depletion mechanism for stratospheric ozone. *Science*, *195*(4275), 287–289. https://doi.org/10.1126/science.195.4275.287

Thorne, R. M., Ni, B., Tao, X., Horne, R. B., & Meredith, N. P. (2010). Scattering by chorus waves as the dominant cause of diffuse auroral precipitation. *Nature*, *467*(7318), 943–946. https://doi.org/10.1038/nature09467

Tong, Y., Vasko, I. Y., Artemyev, A. V., Bale, S. D., & Mozer, F. S. (2019). Statistical Study of Whistler Waves in the Solar Wind at 1 au. *The Astrophysical Journal*, *878*(1), 41. https://doi.org/10.3847/1538-4357/ab1f05

Tsai, E., Artemyev, A., Zhang, X.-J., & Angelopoulos, V. (2022). Relativistic electron precipitation driven by nonlinear resonance with whistler-mode waves. *Journal of Geophysical Research: Space Physics*, *127*(5), e2022JA030338. https://doi.org/10.1029/2022JA030338

Tsurutani, B. T., & Smith, E. J. (1974). Postmidnight chorus: A substorm phenomenon. *Journal of Geophysical Research (1896-1977)*, *79*(1), 118–127. https://doi.org/10.1029/JA079i001p00118

Tu, W., Cunningham, G. S., Chen, Y., Morley, S. K., Reeves, G. D., Blake, J. B., et al. (2014). Event-specific chorus wave and electron seed population models in DREAM3D using the Van Allen Probes. *Geophysical Research Letters*, *41*(5), 1359–1366. https://doi.org/10.1002/2013GL058819

Turner, D. L., Shprits, Y., Hartinger, M., & Angelopoulos, V. (2012). Explaining sudden losses of outer radiation belt electrons during geomagnetic storms. *Nature Physics*, *8*(3), 208–212. https://doi.org/10.1038/nphys2185

Tyler, E., Breneman, A., Cattell, C., Wygant, J., Thaller, S., & Malaspina, D. (2019a). Statistical distribution of whistler mode waves in the radiation belts with large magnetic field amplitudes and comparison to large electric field amplitudes. *Journal of Geophysical Research: Space Physics*, *124*(8), 6541–6552. https://doi.org/10.1029/2019JA026913

Tyler, E., Breneman, A., Cattell, C., Wygant, J., Thaller, S., & Malaspina, D. (2019b). Statistical occurrence and distribution of high-amplitude whistler mode waves in the outer radiation belt. *Geophysical Research Letters*, *46*(5), 2328–2336. https://doi.org/10.1029/2019GL082292

Ukhorskiy, A. Y., & Sitnov, M. I. (2013). Dynamics of radiation belt particles. *Space Science Reviews*, *179*(1), 545–578. https://doi.org/10.1007/s11214-012-9938-5

Verronen, P. T., Marsh, D. R., Szelag, M. E., & Kalakoski, N. (2020). Magnetic-local-time dependency of radiation belt electron precipitation: Impact on ozone in the polar middle atmosphere. *Annales Geophysicae*, *38*(4), 833–844. https://doi.org/10.5194/angeo-38-833-2020

Wang, D., Shprits, Y. Y., Zhelavskaya, I. S., Agapitov, O. V., Drozdov, A. Y., & Aseev, N. A. (2019). Analytical chorus wave model derived from Van Allen Probe observations. *Journal of Geophysical Research: Space Physics*, *124*(2), 1063–1084. https://doi.org/10.1029/2018JA026183

Watt, C. E. J., Allison, H. J., Bentley, S. N., Thompson, R. L., Rae, I. J., Allanson, O., et al. (2022). Temporal variability of quasi-linear pitch-angle diffusion. *Frontiers in Astronomy and Space Sciences, Volume 9, 2022*, *9*. https://doi.org/10.3389/fspas.2022.1004634

Watt, C. E. J., Allison, H. J., Meredith, N. P., Thompson, R. L., Bentley, S. N., Rae, I. J., et al. (2019). Variability of quasilinear diffusion coefficients for plasmaspheric hiss. *Journal of Geophysical Research: Space Physics*, *124*(11), 8488–8506. https://doi.org/10.1029/2018JA026401

Watt, C. E. J., Degeling, A. W., Rankin, R., Murphy, K. R., Rae, I. J., & Singer, H. J. (2011). Ultralow-frequency modulation of whistler-mode wave growth. *Journal of Geophysical Research: Space Physics*, *116*(A10). https://doi.org/10.1029/2011JA016730

Wilson, L. B., III., Cattell, C. A., Kellogg, P. J., Wygant, J. R., Goetz, K., Breneman, A., & Kersten, K. (2011). The properties of large Amplitude whistler mode waves in the magnetosphere: Propagation and relationship with geomagnetic activity. *Geophysical Research Letters*, *38*(17). https://doi.org/10.1029/2011GL048671

Yin, Z.-F., Zhou, X.-Z., Li, W., Shen, X.-C., Rankin, R., Liu, J., et al. (2023). Characteristics of electron precipitation directly driven by poloidal ULF waves. *Journal of Geophysical Research: Space Physics*, *128*(3), e2022JA031163. https://doi.org/10.1029/2022JA031163

Yu, X., Yuan, Z., Wang, D., Allanson, O., & Hunter, S. (2025). Resonance broadening effects of weak turbulence on Earth's radiation belt electrons. *Physical Review E—Statistical Physics, Plasmas, Fluids, and Related Interdisciplinary Topics*, *111*(3), L033201. https://doi.org/10.1103/PhysRevE.111.L033201

Zhang, X.-J., Agapitov, O., Artemyev, A. V., Mourenas, D., Angelopoulos, V., Kurth, W. S., et al. (2020a). Phase Decoherence within intense chorus wave packets constrains the efficiency of nonlinear resonant electron acceleration. *Geophysical Research Letters*, *47*(20), e2020GL089807. https://doi.org/10.1029/2020GL089807

Zhang, X.-J., Artemyev, A., Angelopoulos, V., Tsai, E., Wilkins, C., Kasahara, S., et al. (2022). Superfast precipitation of energetic electrons in the radiation belts of the Earth. *Nature Communications*, *13*(1), 1611. https://doi.org/10.1038/s41467-022-29291-8

Zhang, X.-J., Mourenas, D., Artemyev, A. V., Angelopoulos, V., Bortnik, J., Thorne, R. M., et al. (2019). Nonlinear electron interaction with intense chorus waves: Statistics of occurrence rates. *Geophysical Research Letters*, *46*(13), 7182–7190. https://doi.org/10.1029/2019GL083833

Zhang, X.-J., Mourenas, D., Artemyev, A. V., Angelopoulos, V., Kurth, W. S., Kletzing, C. A., & Hospodarsky, G. B. (2020b). Rapid frequency variations within intense chorus wave packets. *Geophysical Research Letters*, *47*(15), e2020GL088853. https://doi.org/10.1029/2020GL088853

Zhang, X.-J., Thorne, R., Artemyev, A., Mourenas, D., Angelopoulos, V., Bortnik, J., et al. (2018). Properties of intense field-aligned lower-band chorus waves: Implications for nonlinear wave-particle interactions. *Journal of Geophysical Research: Space Physics*, *123*(7), 5379–5393. https://doi.org/10.1029/2018JA025390

Zhao, H., Baker, D. N., Li, X., Jaynes, A. N., & Kanekal, S. G. (2018). The acceleration of ultrarelativistic electrons during a small to moderate storm of 21 April 2017. *Geophysical Research Letters*, *45*(12), 5818–5825. https://doi.org/10.1029/2018GL078582

Zhao, H., Ni, B., Li, X., Baker, D. N., Johnston, W. R., Zhang, W., et al. (2019). Plasmaspheric hiss waves generate a reversed energy spectrum of radiation belt electrons. *Nature Physics*, *15*(4), 367–372. https://doi.org/10.1038/s41567-018-0391-6